2017

LA-6161-PR
Progress Report

NRC-8
Issued: December 1975

HTGR Safety Research Program

July—September 1975

Compiled by

William L. Kirk

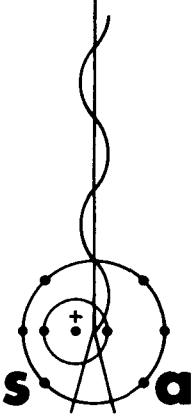

los alamos
scientific laboratory
of the University of California
LOS ALAMOS, NEW MEXICO 87545

An Affirmative Action/Equal Opportunity Employer

UNITED STATES
ENERGY RESEARCH AND DEVELOPMENT ADMINISTRATION
CONTRACT W-7405-ENG. 36

Previous reports in this series, unclassified, are LA-5870-PR, LA-5975-PR, and LA-6054-PR.

In the interest of prompt distribution, this report was not edited by the Technical Information staff.

Work supported by the Reactor Safety Research Division of the Nuclear Regulatory Commission.

Printed in the United States of America. Available from
National Technical Information Service
U S Department of Commerce
5285 Port Royal Road
Springfield, VA 22151
Price Printed Copy $5.50 Microfiche $2.25

DISCLAIMER

CONTENTS

EB

HTGR SAFETY RESEARCH PROGRAM

QUARTERLY PROGRESS REPORT

for

JULY - SEPTEMBER 1975

I. INTRODUCTION

The Los Alamos Scientific Laboratory (LASL) is carrying out a broad program of research in High-Temperature Gas-Cooled Reactor (HTGR) safety technology under the direction of the Reactor Safety Research Division of the United States Nuclear Regulatory Commission. The present LASL program includes the following task areas:

- Fission Product Technology
- Primary Coolant Impurities
- Structural Evaluation
- Safety Instrumentation and Control Systems
- Accident Delineation
- Phenomena Modeling and Systems Analysis

This program was started in March 1974 and is a continuing effort. The present report is the fourth in a series of formal quarterly progress reports.

II. SUMMARY

The effects of a new General Atomic Company (GAC) fuel particle failure model on calculations of ^{131}I release during the Maximum Hypothetical Fission Product Release (MHFPR) accident were studied. The results of comparison calculations substantiate earlier conclusions that the time-dependent release of ^{131}I is nearly independent of the failure model. A Monte Carlo error analysis technique has been applied to the calculation of uncertainty in iodine release during the MHFPR accident. This technique should have many practical applications. Studies of the effects of surface defects on the adsorption of cesium on graphite were continued. Construction has started on the apparatus to be used for studies of the reaction of primary coolant impurities with fission products. When the system has been completed and checked out, experiments concerning the interaction of cesium (in graphite) with water vapor will be initiated.

The OXIDE-3 code received from GAC has been reviewed and rewritten. The revised version, labeled OXIDE-3A, has given results essentially identical to OXIDE-3 for two test problems. Development of the CIMPRE code has been resumed. Modifications to the complex equilibria code QUIL to improve code performance are being carried out. Studies of primary coolant impurity interactions with cesium have been completed. Iodine interactions are now being investigated. Experiments to investigate surface chromium depletion from HTGR metal alloys by impure helium are being carried out. Tentative results indicate considerable chromium depletion during vacuum annealing at 1458 K.

We are proceeding with planning and procurement activities to provide the

capability for earthquake simulation experiments on HTGR core component models. The impact on equipment requirements of earthquake time history scaling has been investigated. The two-dimensional analytical model of the HTGR core has been used to investigate the effects of pin connections between the core blocks on seismic response. Results are summarized in Section V, B1. A prismatic finite element for simulating the 3-D behavior of HTGR core blocks has been developed, and the accuracy of this element has been investigated. We have initiated a study of HTGR core support post stability taking into account static loading and a seismic excitation consisting of both horizontal and vertical components. Progress with NONSAP continues with our current efforts directed toward solving 3-D reinforced concrete test problems.

Study of the possibility of using the release of trapped fission product krypton from HTGR fuel as a post-mortem indicator of the temperature reached by the fuel during irradiation is continuing. A number of questions remain to be resolved. The fundamental question is whether there would be a detectable phenomenon related to exposure temperature. The status of this and other questions is discussed in Section VI.

A framework for carrying out accident delineation has been established. A simple example of the techniques associated with our planned approach is described in Section VII.

A new route for generating neutron cross sections for use in HTGR neutronic calculations has been adopted for the above thermal regime. This new procedure accounts for the double-heterogeneity structure of the HTGR core.

Two-dimensional material worth distributions in the HTGR and isothermal temperature coefficients for compositions approximating the end of equilibrium cycle core have been calculated during this quarter.

The structure of the CHAP code has been revised to accommodate a modular approach to component modeling. A description of the current code package and computing techniques is given in Section VIII.

III. TASK 1, FISSION PRODUCT TECHNOLOGY

A. Effects of the New Fuel Failure Model on the Release of ^{131}I During the MHFPR Accident (J. E. Foley, J. H. Fu, and G. E. Cort)

1. Introduction

The General Atomic Company (GAC) has developed new fuel failure models for both BISO and TRISO fuel particles.[1] The new diagrams for failed fuel fraction versus temperature for accidents involving core temperature transients are given in the GASSAR 6 (Ref. 2) standard safety analysis report. The new fuel failure diagram is shown in Fig. 1; also included in this figure is the earlier fuel failure diagram.[3]

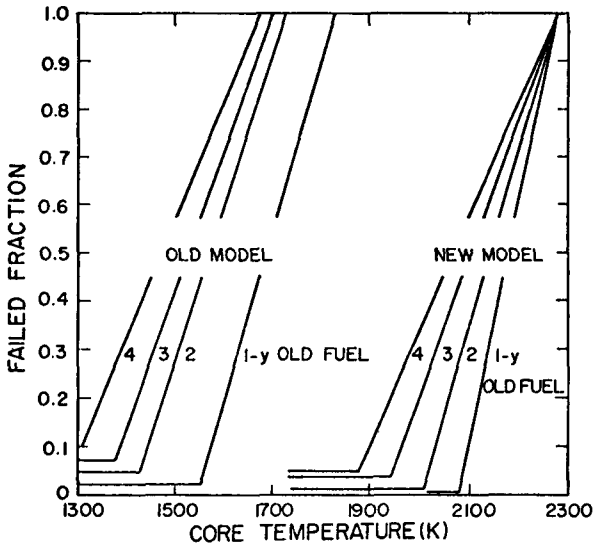

Fig. 1. TRISO fuel particle coating failure diagrams for both the old and new models.

The new failure model exhibits an onset of fuel failure at temperatures much higher than those given by the earlier model. For example, the temperature for 50% failure of 4-yr old fuel has changed from ∿ 1500 K to ∿ 2100 K. Typically, the onset of failure for the new model is 500 K - 600 K higher than that of the earlier model. The onset of fuel failure during the MHFPR accident is thus delayed considerably. The ^{131}I release calculations reported earlier[4] were repeated in order to study the effects of this new failure model on our earlier conclusions.

2. Calculations

The time-dependent release of ^{131}I from an HTGR core was calculated for the MHFPR accident using the AYER heat conduction model.[5] For comparison purposes, release calculations were made using both the old and new fuel failure models. To simplify the calculations, the entire core was assumed to be 2-1/2 yr old. The values of the release constants used in the calculations for failed TRISO fuel were identical to those used earlier (Ref. 4, page 4). An initial failed fraction of 3% was assumed for both calculations. The results of these calculations are shown in Fig. 2.

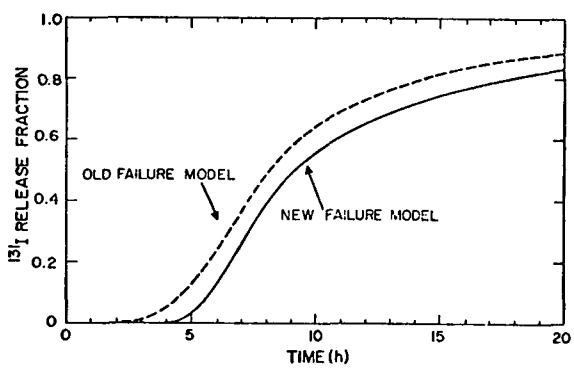

Fig. 2. Time-dependent release of ^{131}I during the MHFPR accident.

3. Conclusions

The results of the calculations using the new fuel failure model indicate that significant ^{131}I release begins ∿ 4 h after the onset of the MHFPR accident; the results from the earlier failure model show the release to begin about 2 h after the onset of the accident. For the new and old failure models, release of 50% of the iodine occurs at ∿ 9 h and ∿ 8 h, respectively, after the onset of the accident. During the time period of maximum release (5 h- 10 h), the new failure model exhibits ∿ 1 h delay in the iodine release. Thus, the large change in the time-dependency of fuel failure, as shown in Fig. 1, is reflected as a much smaller change in the time-dependency of ^{131}I release.

These calculations are in agreement with our earlier conclusions[6] that the time-dependent release of ^{131}I is nearly independent of the fuel failure model, but is strongly dependent on the failed fuel particle release constants.

B. Uncertainty in ^{131}I Release Using Monte Carlo Analysis (G. E. Cort and J. H. Fu)

1. Introduction

A general computer program MCARLO was written to calculate the mean and standard deviation of dependent variables based on stochastic input parameters. The code has been applied to calculate the uncertainty in ^{131}I release from the core of an HTGR following the MHFPR accident. The uncertainty (one standard deviation; 1 σ) after 11 h is ± 18% of the nominal release, caused by the following assumed normally distributed uncertainties (1 σ values):

Decay Power	5%
Weighted Mean Specific Heat	2%
Exponent of Release Constant	0.9%
Pre-exponential Factor for Release Constant	1.5%
Mean Core Density	0.7%

There is theoretically no limit to the number of stochastic variables, their distribution functions, or the complexity of the analytical model. Practical considerations (that is, computer time) will limit the models to those which can be completed in a few minutes of computer time. For 30 trials of the ^{131}I release model described here, the execution time on the 7600 was 5 s.

In applying results such as this to the real world, the major stumbling block is knowing the distribution function for the independent parameters.

2. Discussion

The Monte Carlo technique of error propagation analysis consists of choosing a random value from the distribution function for each of the stochastic independent variables. The calculation is repeated many times (30 to 100), each time with a different array of these variables. The distribution function of the output (dependent) variables can then be used to make statements about the uncertainty in the nominal value or the probability of exceeding some predetermined operating limit. For example, the function $Z = A \cdot B \cdot C$, where A,B,C are normally distributed about some mean value,has a standard deviation σ_Z, given in closed form by:

$$\left(\frac{\sigma_Z}{\bar{Z}}\right)^2 = \left(\frac{\sigma_A}{\bar{A}}\right)^2 + \left(\frac{\sigma_B}{\bar{B}}\right)^2 + \left(\frac{\sigma_C}{\bar{C}}\right)^2 + \left(\frac{\sigma_A}{\bar{A}}\right)^2\left(\frac{\sigma_B}{\bar{B}}\right)^2 + \left(\frac{\sigma_A}{\bar{A}}\right)^2\left(\frac{\sigma_C}{\bar{C}}\right)^2 + \left(\frac{\sigma_B}{\bar{B}}\right)^2\left(\frac{\sigma_C}{\bar{C}}\right)^2 + \left(\frac{\sigma_A}{\bar{A}}\right)^2\left(\frac{\sigma_B}{\bar{B}}\right)^2\left(\frac{\sigma_C}{\bar{C}}\right)^2 \quad (1)$$

where

$\bar{Z}$, $\bar{A}$, $\bar{B}$, $\bar{C}$ are the mean values and σ_A, etc. are the standard deviations.

When the normalized standard deviations, $\frac{\sigma_A}{\bar{A}}$ etc, are small, only the first three terms are significant. In the Monte Carlo method, a random number generator is used to select three values A_i, B_i, C_i from the distributions.

The Monte Carlo model for the HTGR heatup and fission product release used the same main program and logic of selecting random values from the frequency distributions. Instead of the simple three-parameter equation to evaluate, however; a subroutine was added to calculate the transient heatup of the core and resulting iodine release. The model was very similar to the AYER model except for the use of a single average core temperature instead of a finite-element heat conduction mesh. After using this model, it was decided that a three-core temperature model using three decay heating rates would be more exact. The three-region (or more) model is more exact because it is able to simulate the time-dependence of the fuel failure and fission product release more exactly, not because of a need to include heat conduction effects. However, heat conduction to the graphite reflectors is important. This was modeled by an equivalent conductance obtained from the AYER results.

The fuel failure and fission product release were calculated in exactly the same way as in the previous studies,[6] except that only one (average) core temperature was used.

Figure 3 compares average core temperatures by the two methods, with good agreement. The fuel begins to fail much later and is 100% failed much sooner using the single-temperature, MCARLO nominal model (Fig. 4). This is due to the range of core temperature levels in the finite-element code. The nominal iodine release rate (Fig. 5) does not begin to catch up to the AYER result until about 10 h after the

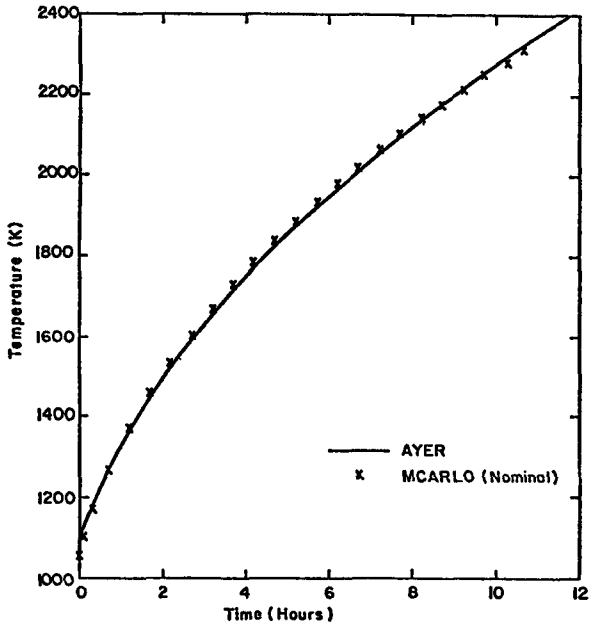

Fig. 3. Average core temperature.

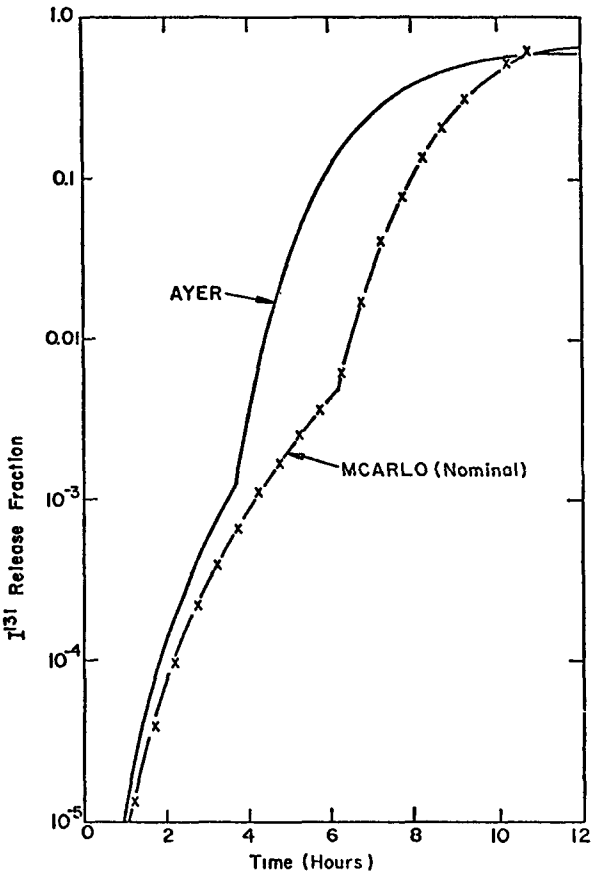

Fig. 5. Iodine - 131 release.

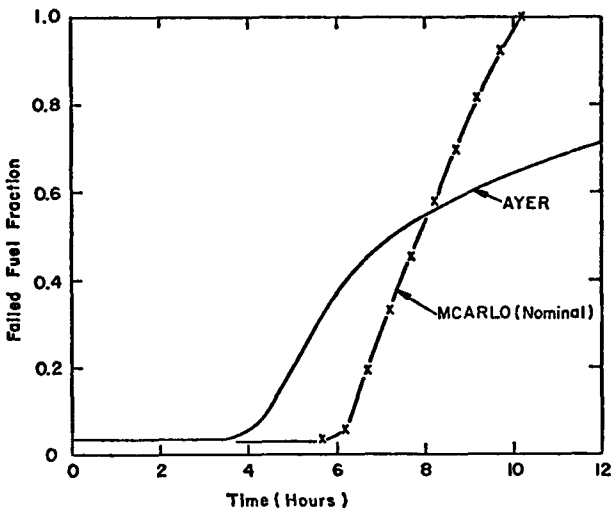

Fig. 4. Fuel failure fraction.

accident. A three (or more) temperature model could be derived from the existing single element model and would take proportionally longer to run on the computer.

For the 30 trials, Table I gives the maximum and minimum values for the stochastic variables.

3. Conclusions

The technique of using a complicated model to predict nominal behavior and a simplified one for Monte Carlo uncertainty analysis should have many practical applications. For many real systems, the propagation of error analysis can be done in no other way. If distribution functions other than normal must be included, they are easy to apply by selecting the random numbers from the appropriate distribution. The uncertainties can be

TABLE I

MAXIMUM AND MINIMUM VALUES OF THE STOCHASTIC VARIABLES

Parameter	Nominal	Maximum	Minimum
Relative decay power	1.0	1.084	0.919
Relative core weighted mean specific heat	1.0	1.058	0.961
Exponent of release constant	-22075.6	-21599.	-22377.
Pre-exponential factor for release constant	6796.7	6958.	6669.
Mean core density	1457.6	1473.7	1429.1
^{131}I release fraction at 10.7 h	0.611	0.893	0.310

allowed to change with time, temperature, or some other parameter. For example, the decay heating can become increasingly less accurate at longer times and the specific heat less accurate at higher temperatures.

Information as to the uncertainties in core temperature and iodine release as functions of time can be obtained with no significant increase in complexity or computer time.

When the modeling is done carefully, the relative error from the simplified Monte Carlo analysis should apply (within definable error bounds) to the results of the complete (complicated) model.

The standard deviations in the independent variables must be obtained from literature search, experiment, previous analysis, or (frequently) engineering judgement. General Atomic Company[7] used a 10% "conservative" increase in decay power which we took to represent a 2 σ value. The other uncertainties used in this report are engineering estimates.

C. Effect of Surface Defects on the Adsorption of Cesium on Graphite (B. L. Holian)

In the previous quarterly report (Ref. 4, page 11), the interaction of a cesium ion with a perfect graphite surface was presented. Using the resulting potential, preliminary dynamic calculations indicated that the migration of cesium on a perfect graphite surface is like that of a free two-dimensional particle for temperatures above about 1000 K. Thus, true surface diffusion of cesium on graphite requires the presence of surface defects which could be either attractive or repulsive sites for motion parallel to the surface. Such defect sites, if more attractive than a perfect surface, could also give rise to a higher calculated adsorption energy for the low surface coverage limit (Henry's Law regime).

The effect of missing carbon atoms in the graphite surface ("holes" or "pits") upon the adsorption energy of cesium is dramatic, as shown in Table II (the method of calculation has been presented in Ref. 4). The adsorption energy is given as a function of the size of the pit in the graphite surface. Three carbon-carbon bonds must be broken for the first missing carbon atom (see Fig. 6). The one-atom hole is repulsive by one-half kilokelvin relative to the perfect surface. For the next carbon atom to be removed, two bonds must be broken (see Fig. 7). The two-atom hole is attractive by two-kilokelvin. With four adjacent carbon

TABLE II

ADSORPTION ENERGY OF CESIUM OVER HOLES IN THE GRAPHITE SURFACE

Number of missing C atoms	Number of broken C-C bonds/missing C atom	$-\frac{\Phi}{k_B}$ (kK) [a]	Z (Å) [b]
0	0	61.3	2.97
1	3.00	60.8	2.92
2	2.50	63.2	2.61
4	2.25	70.4	2.11
6	2.00	102.0	1.40
24	1.75	99.0	1.26
∞	1.50	-	-

[a] Potential energy, R_{max} = 14.5 Å (k_B = Boltzmann's constant).

[b] Height of cesium ion above graphite surface for minimum in potential energy.

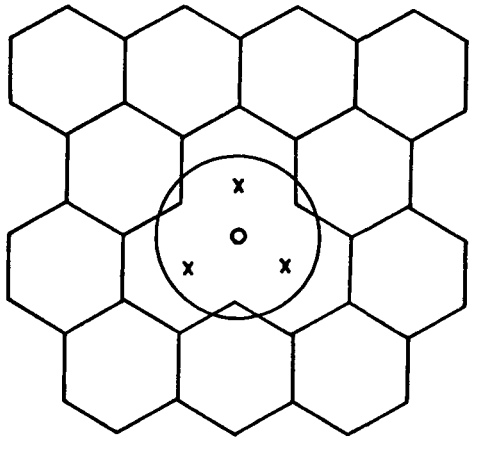

Fig. 6. One-atom defect in a graphite surface. (—— = carbon-carbon bond with r(C) = 1.421), o = position of missing carbon atom, x = equilibrium positions of Cs^+ ion, large circle with r(Cs^+) = 1.69 Å shows size of ion compared with hole in graphite surface).

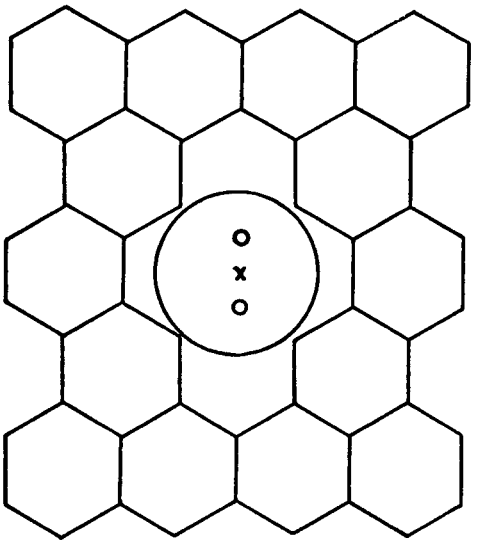

Fig. 7. Two-atom defect in a graphite surface. (same key as Fig. 6)

atoms missing, three different shapes are possible (the one with trigonal symmetry is shown in Fig. 8. The four-atom hole is attractive by about nine kilokelvin. A noticeable transition occurs when the hexagonally-symmetric six-atom hole is made from the five-atom hole by breaking only one more C-C bond* (see Fig. 9). At this point, the Cs^+ ion is just able to squeeze down comfortably into the hole at a height above the graphite surface not far from the conducting plane (Z_o = 1.28 Å). As the number of missing atoms is increased, very little effect is seen, though the minimum energy rises slightly by the 24-atom hole, the next hexagonally-symmetric hole after the 6-atom hole (see Fig. 10). The reason for the higher energy is the Cs^+ can get close to the carbon atoms at the edge of the 24-atom hole, while in the 6-atom hole, the Cs^+ is completely surrounded by carbon neighbors. The atoms below the first layer do not have a great effect on the potential energy, as verified by calculations of the six-atom hole with one and four atoms missing from the sublayer. The conducting plane, which contains the donated Cs electron, serves to hold the Cs^+ at $Z \sim z$ (see Eq. 16 of Ref. 4), at least in this model.

In order to draw a firm conclusion from these results for a defective graphite surface, molecular dynamics calculations of thermal annealing of the surface ought to be carried out. Such computer experiments might show the coalescence of randomly distributed one-, two-, ..., and five-atom pits into six-(or more) atom pits, thereby yielding a realistic

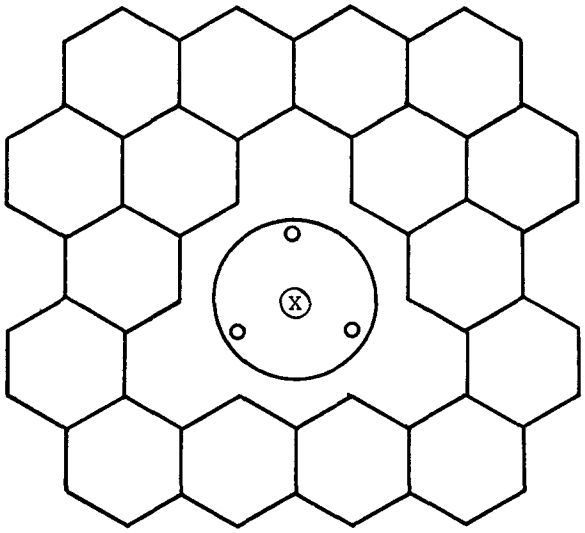

Fig. 8. Four-atom defect in a graphite surface. (same key as Fig. 6)

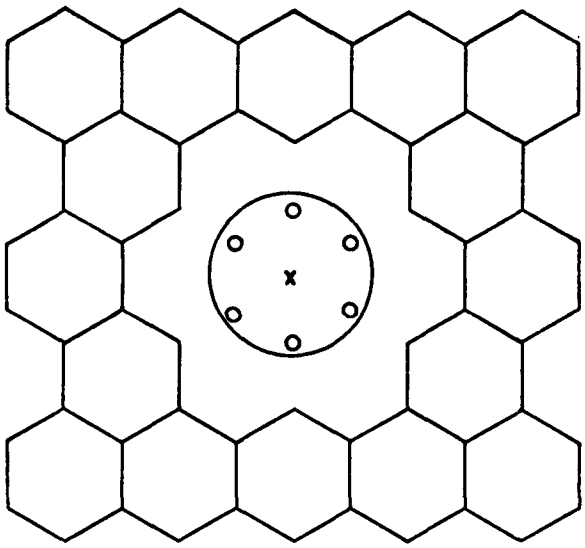

Fig. 9. Six-atom defect in a graphite surface. (same key as Fig. 6)

*By this simplified thermochemical argument, we mean to illustrate the distinct energetic preference for 6- (or more) atom holes over a random distribution of smaller holes in a graphite surface (see Table II for number of C-C bonds broken per missing carbon atom as a function of the number of atoms comprising a hole).

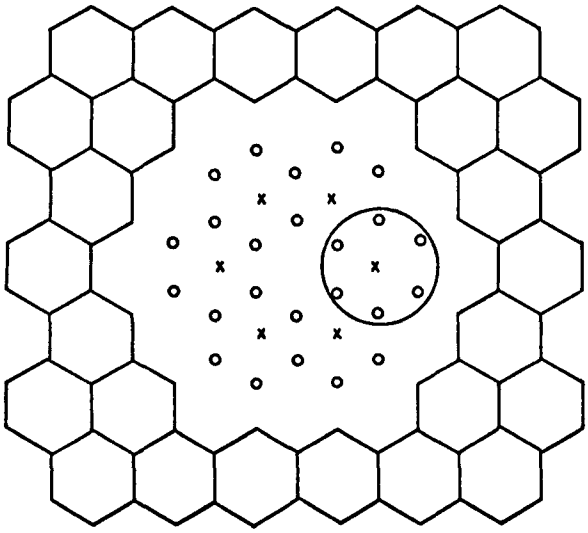

Fig. 10. 24-atom defect in a graphite surface. (same key as Fig. 6)

surface defect distribution. Then, by following the motion of a cesium ion on this more realistic surface, a surface diffusion coefficient, as well as average adsorption energy, could be calculated, essentially from first principles, and compared with the recent experimental results.

D. Primary Coolant Impurities Interactions with Fission Products

W. A. Stark

A start has been made on the construction of the apparatus intended for studying the reactions of primary coolant impurities with fission products. A block diagram of the apparatus is shown in Fig. 11; the portion within the dashed boundary has been completed and is undergoing leak checking.

The system is essentially all metal to allow operation at pressures greater than one atmosphere and to allow at least partial bakeout of the gas delivery lines to maintain gas atmosphere purity. As presently configured, the gas delivery system includes a main helium supply line, and two impurity injection lines. The latter contain electronic gas flow

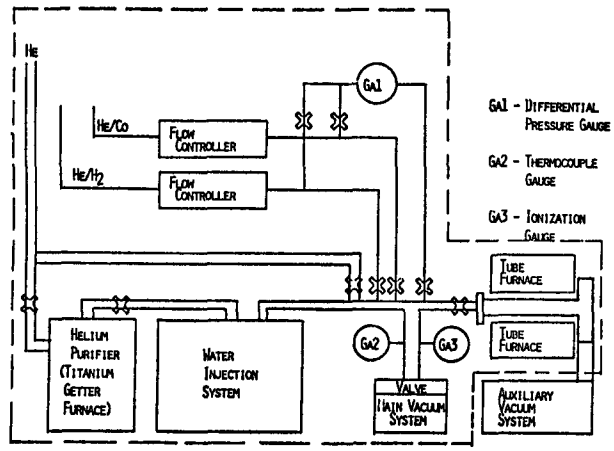

Fig. 11. Block diagram of coolant impurities apparatus.

monitoring and control valves which deliver 1% CO or H_2 in helium mixtures to the main gas line.

The main helium is purified of oxidants by a titanium bed at a temperature of $\sim$ 1050 K; if desired, precise water injection is accomplished by passing the main stream helium through a water electrolysis cell. The effluent gases (He, H_2, O_2, and H_2O) are then passed through a liquid nitrogen trap which condenses the H_2O. The resulting He containing H_2 and O_2 is subsequently passed over a hot platinum gauze catalyst, where the H_2 and O_2 recombine to give water vapor. Knowledge of the electrolysis current and the flow rate of the helium gas gives the water vapor concentration.

Following leak checking, the performance of the titanium getter furnace, the water injection system, and the CO and H injection system will be evaluated using the helium after-glow moisture and impurity monitoring device (Ref. 4, p. 37-39).

When satisfactory performance of the gas delivery system is demonstrated, experiments will be initiated to study the interaction of low levels of water vapor with cesium in graphite. Reactions will be

monitored using either a microbalance system or a quartz crystal oscillator system.

IV. TASK 2, PRIMARY COOLANT IMPURITIES

Efforts within this task area are directed to the analytical and experimental study of the interactions between impurities in the helium primary coolant gas and the various materials in the primary coolant circuit. The more likely impurities are steam, and the products of the steam/graphite reaction: hydrogen, carbon monoxide, carbon dioxide, or methane. Materials of interest include the core and related graphite structures, and metallic components such as steam generators, helium circulators, orifice valves, and control rod systems. Interactions between gaseous impurities and fission products are also of interest.

A. Code Development (A. Bowman, R. Feber, and J. Lundsford)

The OXIDE-3 code received from GAC has been reviewed and rewritten in a different style. The modified version, designated OXIDE-3A, is now fully operational, and has been tested with a design steam leak problem and with a depressurization accident problem. The two code versions give essentially the same answers, with most computed quantities agreeing to within 1%. The pressure drop across the core is calculated and maintained in OXIDE-3A. The resultant effect is practically negligible, less than 0.5% on all output quantities for the design steam leak problem. The BLDG subroutine has been modified extensively, with the correction of some programming errors and a change in the time integration logic. The effect on building conditions is of the order of 1-3% in the depressurization accident.

The development of the CIMPRE code has been resumed. The method for coupling heat transfer and the diffusion of reacting chemical species is under study at present.

Effort is being expended upon certain modifications to the complex equilibrium code, QUIL. In all problems for which solutions have been obtained, the solution minima have been well behaved. However, instances have occurred in which the trajectory in parameter space brings the system solver into a singular region when still far removed from the solution minimum. Computing effort increases considerably at this point, and in some cases no solution is obtained. It is hoped that performance can be improved by a modification of the search strategy embedded in the subroutine DSER. As a first step, DSER is being further broken down into other subroutines to provide a more flexible logic pattern in the direct search phase. It is then hoped that further study can indicate remedies for this problem.

Calculations are continuing on the chemical interaction of the primary coolant loop impurities with fission products. The initial effort was directed toward cesium; a topical report is in the rough draft stage and treats the equilibrium behavior of cesium species during a variety of normal, off-normal, and accident HTGR operating conditions.

The next elements to be investigated will be tellurium, iodine, and strontium. Unfortunately, the thermochemistry of these elements is not as well established as for cesium, and considerable effort is required in order to secure the literature data. Since iodine is better characterized than either tellurium or strontium, it was decided to investigate this element next. To date, using a limited thermodynamic data base, no condensed iodine compounds have been found that would be stable in the reactor environment. Some solubility would have to exist in the complex carbides present in the fuel bead, although this may represent an insignificant amount. Concentration distributions have been calculated on the basis of gaseous compounds for which thermodynamic

data have been located. These compounds include the monomer and dimer of iodine, hydrogen iodide, cyanogen iodide (ICN), and nitrosyl iodide (ION).

Figure 12 is an activity plot of these species at equilibrium in the Peach Bottom stoichiometry. The stable iodine species are seen to be hydrogen iodide at low temperatures, and the monomer of iodine at higher temperatures. The transition temperature is about 1050 K. The distributions of the components are little changed by the absence or presence of carbon. Calculations are being carried out to determine the effect of the different reactor stoichiometries upon the distribution of species present.

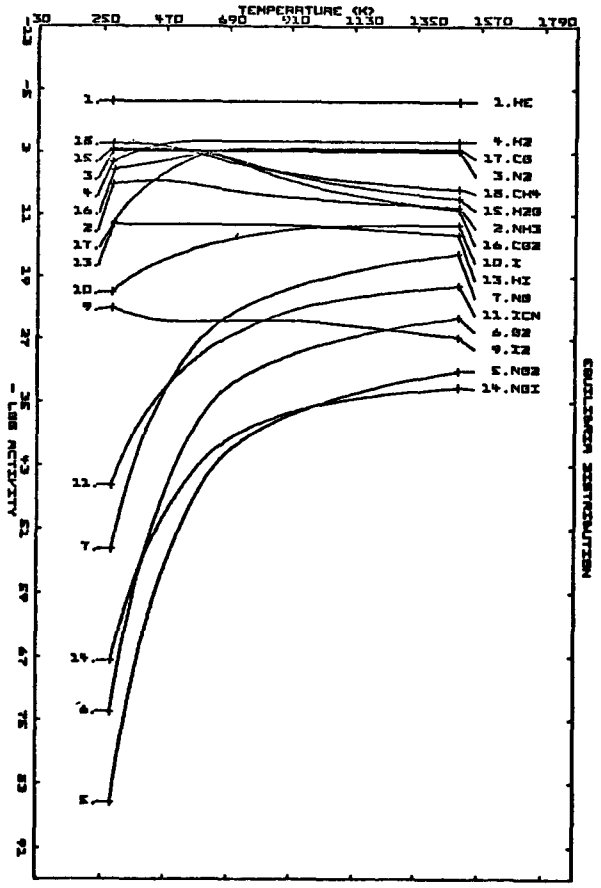

Fig. 12. Equilibrium distribution of species of iodine present in the Peach Bottom stoichiometry. Excess carbon present, and iodine at 10^{-10} ppmv. Total pressure 2296 kPa.

B. Coolant Impurity Reactions with Graphite and Metallic Components (L. C. Michels and W. A. Stark)

Prior work[8-11] has shown that austenitic alloys such as the stainless steels, incoloys, and inconels exhibit depletion of certain alloying elements during long-term exposure to impure helium at elevated temperatures. This depletion occurs in the metal layer immediately beneath a porous, nonprotective oxide film that forms on the alloy surface. Depletion is a result of the selective oxidation and concentration of chromium, titanium, and manganese in the surface oxide. The depleted layer has been reported to be about 2-5 times as thick as the surface oxide. Aside from possible mechanical property deterioration due to this depletion, a consequence with implications for reactor safety is the loss of oxidation resistance.

The normally excellent oxidation resistance of these alloys is due largely to their high chromium content. In atmospheres with high oxidant levels, a thin, compact, and adherent film quickly forms on the surface of the alloy. This film is basically some modification of Cr_2O_3, and acts as a diffusion barrier to protect the alloy from further rapid oxidation.

During long term exposure to HTGR helium these alloys generally do not form a protective oxide film. Additionally, it is possible they may loose their resistance to oxidation due to chromium depletion. In the event of a reactor accident after long-term normal operation and during which high levels of oxidant are introduced into the primary circuit, rapid internal oxidation of these alloys could occur. This in turn might cause embrittlement and increased fracture sensitivity. Subsequent operation of the reactor could then result in premature failure of the affected components.

Experimental work is in progress to simulate in a short time the alloy

depletion that occurs during long term exposure of alloys to impure helium. Such specimens can then be exposed to coolant impurity conditions believed to exist during reactor accidents in order to determine the effects of prior alloy depletion.

In some preliminary studies, specimens of Incoloy 800 wire of nominal 0.5 mm diam were annealed at 1173 K and 1458 K in a vacuum of 10^{-5} torr. The purpose of this treatment was to remove alloying elements such as chromium and titanium from the surface layers of the specimens by evaporation. The specimens, including as-received material were then exposed to flowing air at 973 K and atmospheric pressure. Subsequent metallographic examination showed differences in oxidation behavior.

The samples annealed at 1173 K showed no observable differences in oxidation when compared to the as-received material. The expected oxide films were apparently too thin to be seen at magnifications up to 600 X. The sample annealed at 1458 K, however, showed large patches of relatively thick oxide that had penetrated into the base metal (see Figs. 13 and 14). Other microstructural changes occurred, such as grain growth and intergranular carbide precipitation. These are believed to be strictly thermally induced changes unrelated to the observed oxidation behavior.

On the basis of these observations, it appears that appreciable depletion of chromium took place during vacuum annealing at 1458 K, but not at 1173 K. It further appears that this depletion resulted in enhanced oxidation. Confirmation of these tentative conclusions awaits the results of electron microprobe analysis of the specimens.

It would be desirable to correlate the concentration profiles developed using this simulation method with those brought about by long-term exposure to impure HTGR helium. Although such information is available in the literature, it is by no means extensive. An attempt to establish or estimate such a correlation will be the subject of further inquiry along with continuing experimental efforts.

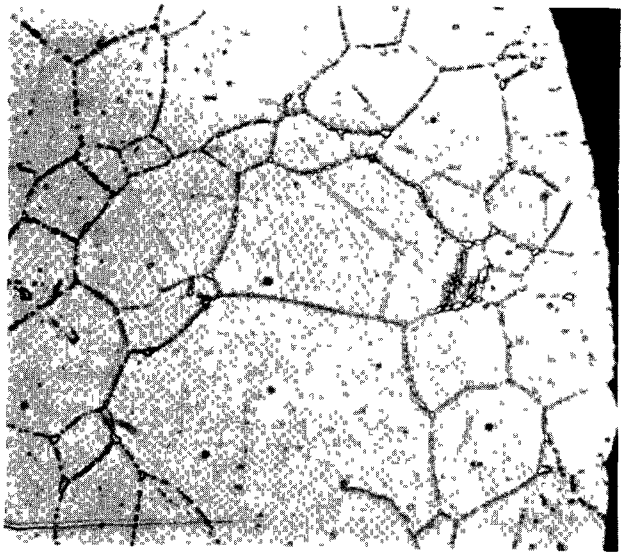

Fig. 13. Air oxidation of Incoloy 800. 600X. Pretreatment: 1173K, 10^{-5} torr, 48 h. Air exposure: 973 K 0.78 atm, 8 h. Etch: Glyceregia 30 s.

Fig. 14. Air oxidation of Incoloy 800. 600 X. Pretreatment: 1458 K, 10^{-5} torr, 1 h. Air exposure: 973 K, 0.78 atm, 8 h. Etch: Glyceregia, 90 s.

V. TASK 4, STRUCTURAL INVESTIGATION

A. Physical Model Test Program for Core Seismic Response (R. C. Dove and C. A. Anderson).

1. Physical Test Facility

A request for a proposal for the servohydraulic shaker to be purchased for the physical test laboratory has been prepared. Our present plans are that initially the shaker will provide only for controlled horizontal table motion with excitation in the frequency range from 0.1 to 100 Hz. In addition to specifications in terms of frequency versus motion capabilities, the vendors have been requested to specify the shaker's capabilities to reproduce a random motion (recorded or simulated earthquake) specified in terms of that motion's response spectrum. The random motion which it is desired to produce is specified in terms of the response spectra discussed in Section 2 below and shown, for example, by Figs. 15, 16, and 17. After contact

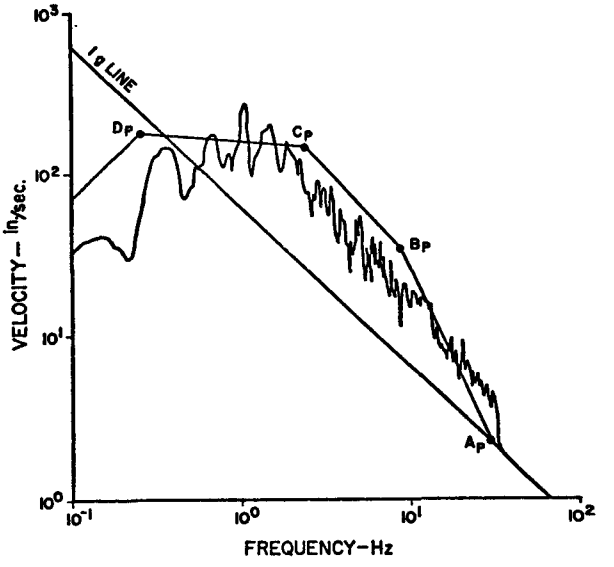

Fig. 16. Response spectrum of simulated earthquake for prototype testing.

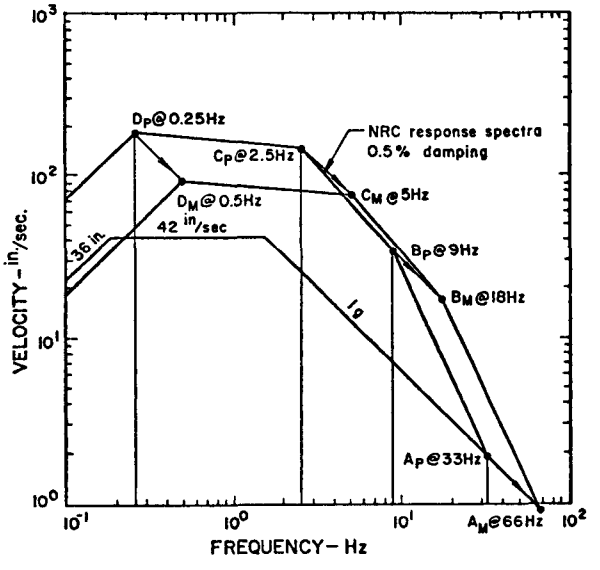

Fig. 15. Shifting of model response spectrum.

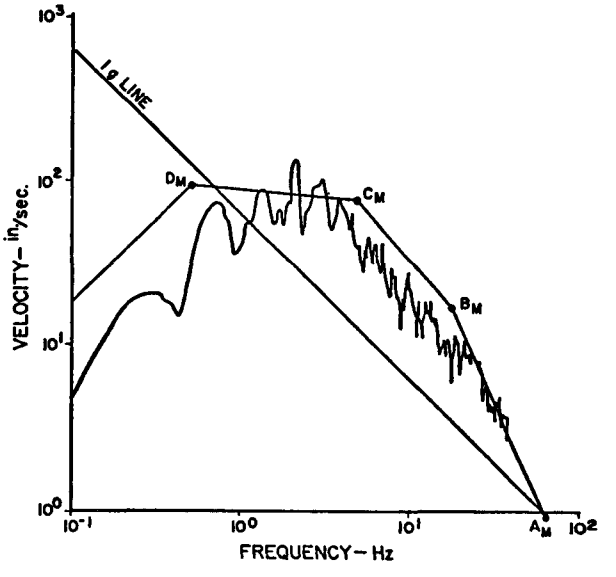

Fig. 17. Response spectrum of frequency shifted simulated earthquake.

with the vendors we will write a final purchase order that will be placed as soon as funding is available.

2. Investigation of Earthquake Scaling

As part of preliminary planning for physical testing of scale models some investigations have been made in the scaling of earthquake time histories.

Anticipating the "Froude" scaling[12] (that is, the effect of gravity included) will be appropriate,we expect that the following scale factors will be required:

a. Time Scale (N_t)

$N_t = \sqrt{N_d}$, where N_d is the desired length scale.

b. Velocity Scale (N_v)

$N_v = \sqrt{N_d}$

and

c. Acceleration Scale (N_a)

$N_a = 1$.

Since the simulated earthquake used for driving test models will be specified in terms of their response spectra it is useful to compare the NRC required spectrum to its equivalent scaled value. This is done in Fig. 15, where a length scale (N_d) of four has been assumed. The piecewise linear curve marked $A_pB_pC_pD_p$ represents the NRC required response spectrum (0.5% damping) for a simulated earthquake to be used in a prototype test. The piecewise linear curve marked $A_mB_mC_mD_m$ represents the required spectrum (0.5% damping) for a simulated earthquake to be used in a model test where the length scale has been selected as four, that is, $N_d = 4$. Clearly all points have been time shifted so that frequencies are doubled ($N_t = \sqrt{N_d} = 2$; that is, model periods are halved or frequencies doubled) and accelerations for homologous frequencies remain constant.

The response spectrum of the simulated earthquake previously used to drive our analytical models is shown in Fig. 16 and the response spectrum for the scaled ($N_d = 4$) version of the same earthquake is shown in Fig. 17. Clearly, it is not difficult to properly scale the earthquake history, but all equipment and instruments used to treat and measure this signal must have adequate capability over the new frequency range. In this example we note that the spectrum analyzer does not have capabilities to the required 66 Hz.

B. Analytical Model Development for Core Seismic Response (J. G. Bennett, R. C. Dove, K. H. Duerre, J. L. Merson and C. A. Anderson)

1. Two-dimensional Core Seismic Model

As indicated in the previous quarterly progress report a two-dimensional analytical model of the core had been made operational. During this quarter this model has been run to investigate the effect of the pin connections between core blocks on the system's seismic response. The model and forces considered are shown in Figs. 18 and 19. In all of the computations made using this two-dimensional model the values of block stiffness and pin stiffness used were those obtained from the analysis reported on in the previous quarterly progress report. Model parameters used as "base" data are given in Table III. The excitation consisted of a horizontal base acceleration of amplitude 1g and frequency 5 Hz. The vertical base motion was zero.

Output available for each block (in both tabulated and plotted form) includes: horizontal acceleration versus time; contact force on block side walls versus time; pin force versus time; vertical acceleration versus time; and contact force on block bases versus time. Figure 20 gives an example for a 1-s run using base data. Vertical accelerations and forces are not shown in this case since the vertical input was zero.

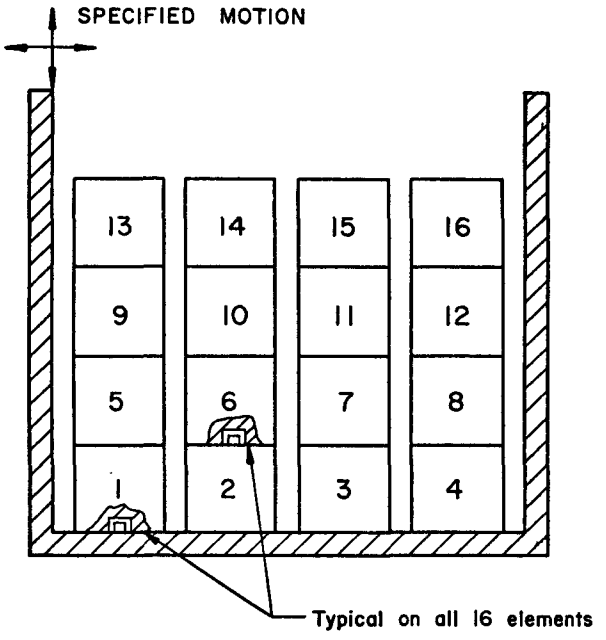

Fig. 18. Two-dimensional model.

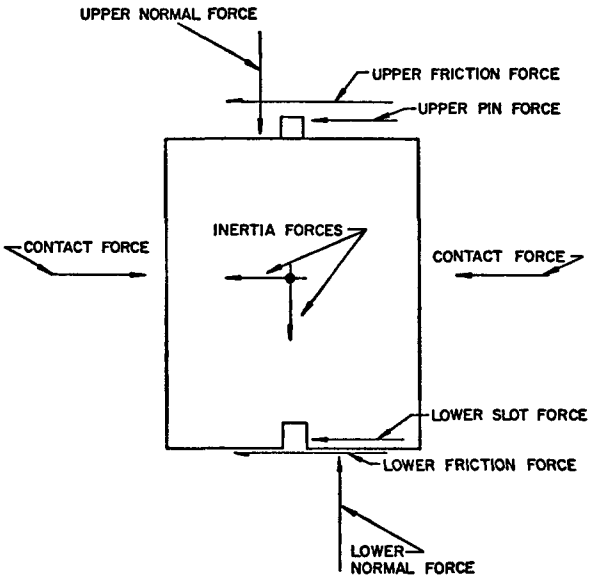

Fig. 19. Free body diagrams illustrating all effects in the two-dimensional model.

TABLE III

BASE VALUES USED IN THE STUDY OF THE TWO-DIMENSIONAL MODEL

Item	Symbol	Base Value
Block Size	d	0.38 m (15-in.)
Block Weight	W	794 N (178.5 lb)
Block Stiffness		
Horizontal Direction	K_H	1.89×10^9 N/m (10.8×10^6 lb/in.)
Vertical Direction	K_V	2.84×10^9 N/m (16.2×10^6 lb/in.)
Connector Stiffness		
Pin	K_p	1.084×10^9 N/m (6.19×10^6 lb/in.)
Slot	K_s	1.084×10^9 N/m (6.19×10^6 lb/in.)
Gap Between Block	C	3.8 mm (0.150-in.)
Clearance Between Pin & Slot	h	1.27 mm (0.050-in.)
Friction Between Horizontal Surfaces		
Static Coefficient	μ_s	0.20
Kinetic Coefficient	μ_k	0.16

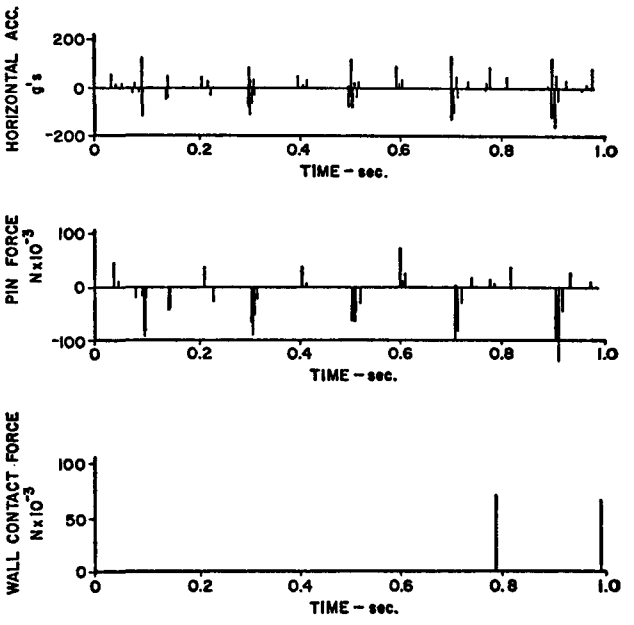

Fig. 20. Response of block #9 to horizontal sinusoidal excitation.

The general behavior of the pin restrained, two-dimensional system can be explained in terms of these figures. Although block number 9 received 61 acceleration pulses (see the top response in Fig. 20), only two of these are due to side wall impacts (see the bottom response in Fig. 20). The remaining pulses result from pin-slot closure; those applied to the base of block number 9 are shown as the middle response of Fig. 20 and those applied to the top of block number 9 are available as the equal, but opposite, reactions of the lower pin forces on block number 13.

A series of runs have been made in which pin clearance (h) and pin stiffness (K_p and K_s) have been varied from the base values. The results may be summarized as follows:

a. Side contact between blocks is eliminated in all horizontal rows below which the accumulated pin gap clearance is less than the gap between blocks.

b. Smaller pin/slot clearances (lower h) produce more numerous, but less intense pin/slot impacts.

c. Stiffer pins (higher values of K_p or K_s) produce more numerous and more intense pin/slot impacts.

Results from several specific runs are summarized in Table IV.

During the coming quarter this two-dimensional model will be used to investigate the effect of vertical input on system accelerations and forces.

2. Investigation of the Damping Mechanisms Being Used in the One-and Two-dimensional Analytical Models

During the RSR-HTGR structural review* one of the participants suggested that perhaps the importance of system damping which was indicated by studies conducted on our analytical model was in reality due to "computational damping" associated with the numerical method being used. To demonstrate that our model behavior is indeed due to the frictional damping and/or the hysteretic energy loss assigned to the system rather the "computational damping", three runs were made on the one-dimensional, four-block model.[4]

For the first run the model was assigned zero frictional damping and zero hysteretic energy loss. The system was excited by a 1 g, 5 Hz base motion for 0.4 s; following this the base excitation was reduced to zero. Figure 21 indicates that system motion continues after base motion ceases with essentially no damping. In the second run the system was assigned a coefficient of kinetic friction of 0.16. Figure 22 indicates that system motion

*This review was held by NRC at Germantown, Maryland, on June 12, 13, 1975.

TABLE IV

EFFECT OF PIN CLEARANCE AND STIFFNESS

Description[a]	Max. Block Acceleration(9)	Max. Side Contact Force (N)	Max. Pin Shear Force (N)
1-D System (Block 1,2,3,4, only), no pins	345	274×10^3 (61 677 lb)	---
2-D System (Block 1-16) no pins	377	299×10^3 (67 281 lb)	0
2-D System Base Values	178	131×10^3 (29 520 lb)	140×10^3 (31 597 lb)
2-D System h decreased to 0.254 mm (0.010 in.)	72	0 (no side contact)	57×10^3 (12 879 lb)
2-D System h increased to 0.254 mm (0.100 in.)	327	260×10^3 (58 344 lb)	169×10^3 (38 006 lb)
2-D System K_p and K_s increased to 1.75×10^9 N/m	219	128×10^3 (28 820 lb)	173×10^3 (38 966 lb)
2-D System K_p and K_s decreased to 0.7×10^9 N/m	164	130×10^3 (29 200 lb)	115×10^3 (25 907 lb)

[a]All values are as given in Table III except as noted.

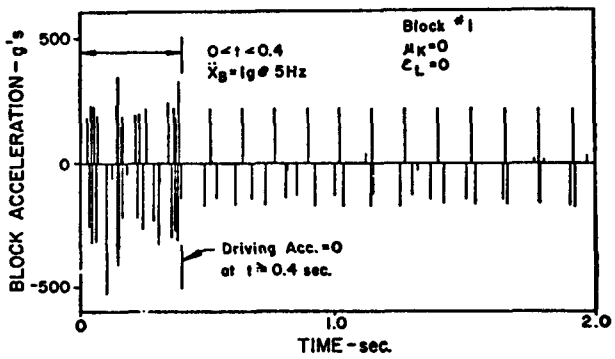

Fig. 21. Undamped response of four-block model.

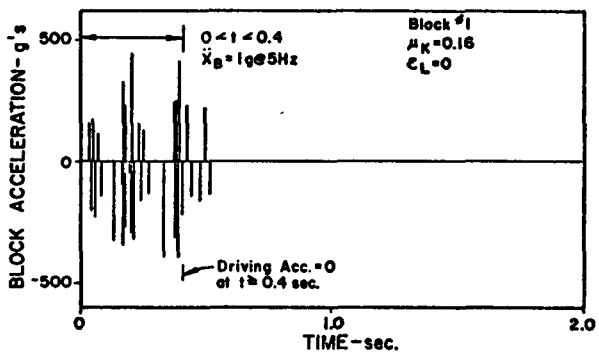

Fig. 22. Response of four-block model with coefficient of kinetic friction equal to 0.16.

is rapidly reduced to zero after base motion ceases. In the third run the system was assigned zero frictional damping and a hysteretic energy loss of 40%. Figure 23 indicates the effect of this type of damping.

3. Fuel Block Locating Pin Slot Stiffness

The fuel block locating pin is restrained in its lateral movement by a circular slot in an adjacent fuel block or support material. Three finite element models were used in estimating the stiffness of the slot. They were:

a. Model I, (Fig. 24) similar to that used for pin stiffness estimates reported earlier.[4] This model was analyzed by the SABOR/DRASTIC computer code.

b. Model II, indentical to Fig. 25 except for the truss elements that were not included.

c. Model III, shown in Fig. 25. Both Model II and III used the plane strain option of computer program SAP-IV.

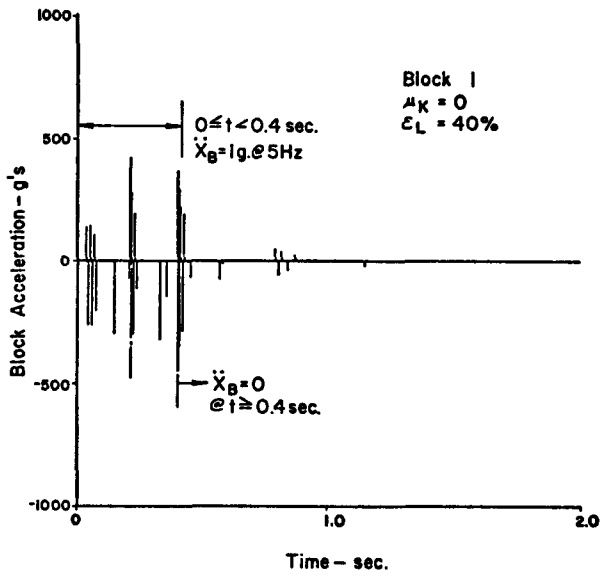

Fig. 23. Response of four-block model with hysteretic energy loss.

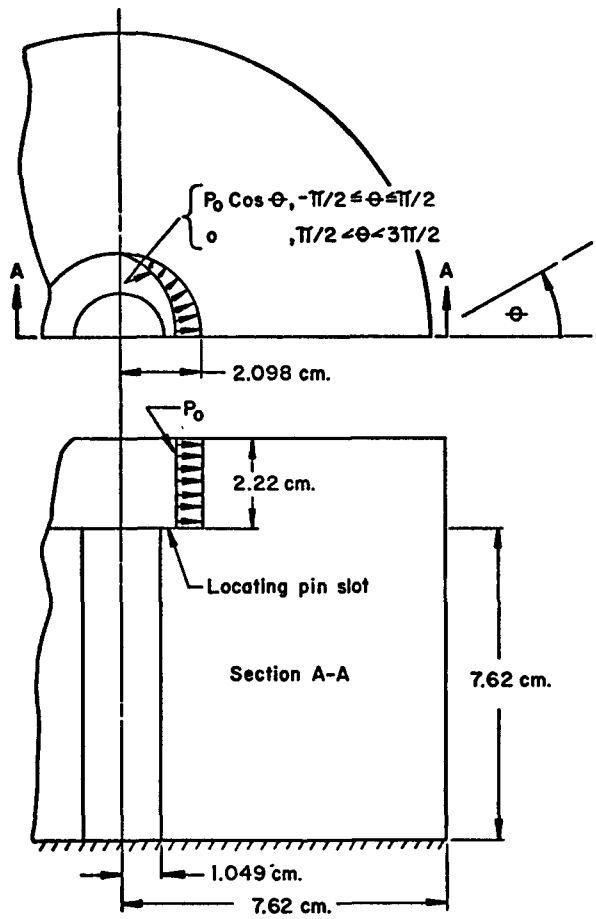

Fig. 24. Axisymmetric model for pin slot stiffness calculation.

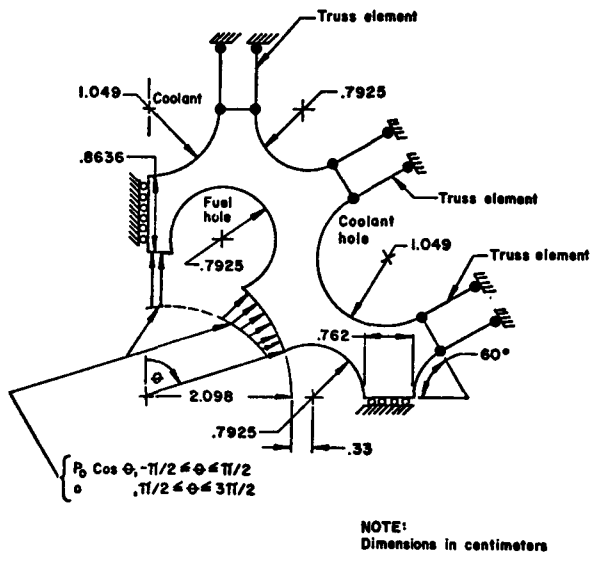

Fig. 25. SAPIV finite element model for pin-slot stiffness calculation.

A half-cosine static load was assumed for all three representations. This was accomplished by specifying the Fourier components for the SABOR version and by obtaining the nodal forces for Models II and III by integrating the pressure times the nodal area, that is:

$$F_n = \int Pda = P_o R_o \int_{\theta_1}^{\theta_2} \cos\theta d\theta \qquad (2)$$

where R_o, θ_1 and θ_2 define the area associated with the nodal force.

Model I gave a value of stiffness of 2×10^9 N/m as an upper limit since the coolant and fuel holes were not removed from the material. A stiffness value of 4×10^7 N/m was obtained from Model II; however, unreasonable (negative) displacements were also obtained. Consequently truss elements were added. The elastic modulus of the trusses was obtained from the relation $E = K \cdot \ell/A$, by fixing the length and cross sectional area and assuming the same stiffness as the fuel block. This third model gave an intuitively reasonable value of 3×10^8 N/m for stiffness of the slot. The last estimate is 30% of the pin stiffness versus 200% and 3.5% for Models I and II respectively.

4. Development of a Prismatic Finite Element

Attempts to model the dynamic behavior of HTGR cores have relied, in general, on modeling by discrete springs and point masses. Values of the spring constants and point masses are determined in many cases by ad hoc methods which do not take into account the structure of the bodies involved. The finite element method provides a way of treating individual structural elements, such as fuel blocks, for determination of spring stiffnesses and equivalent masses. These stiffnesses and masses can later be used with a time integration routine to calculate the dynamic response of the assembled structure. In addition to providing a method of determination of spring stiffness and equivalent point mass, the finite element method also yields the stress variation in the individual element with but a small amount of additional calculation.

The ability of any finite element to accurately describe its various modes of deformation depends on the order of the approximating shape functions. For predicting core block behavior we felt that the shape functions should allow for extension, torsion, pure bending, and bending in the presence of transverse shear stress. Figure 26 shows an idealized (without coolant holes, etc) model of a graphite core block; the hexagonal core block is made up of six subelements of triangular cross sections as shown. We have taken shape functions in the subelement which are linear through the cross section and quadratic along the length of the cylinder; these shape functions allow the subelement to undergo the aforementioned deformation modes. The shape functions for the triangular prism are given by the following expressions:

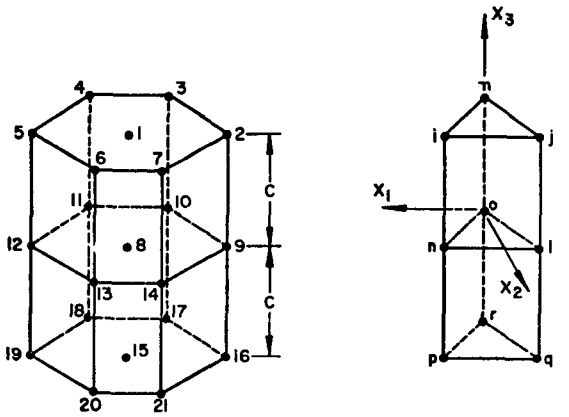

Fig. 26. 21 node hexagonal prism and basic subelement.

$$x_3 = +c: \quad N_i(x_1, x_2, x_3) = \frac{1}{2} L_i(x_1, x_2)\left(\frac{x_3}{c}\right)\left(1 + \frac{x_3}{c}\right), \quad i = 1,2,3$$

$$x_3 = 0: \quad N_i(x_1, x_2, x_3) = \frac{1}{2} L_i(x_1, x_2)\left(1 - \frac{x_3^2}{c^2}\right), \quad i = 1,2,3 \qquad (3)$$

$$x_3 = -c: \quad N_i(x_1, x_2, x_3) = \frac{1}{2} L_i(x_1, x_2)\left(\frac{x_3}{c}\right)\left(\frac{x_3}{c} - 1\right), \quad i = 1,2,3$$

where $L_i(x_1, x_2)$, $i = 1,2,3$, are the linear shape functions for the plane triangle (see Ref. 13, Chapter 4) and c is the prism half-length. From Eq. (3) the strain-displacement matrix can be obtained. Using the elastic constitutive matrix for transversely isotropic materials as a model for graphite behavior, we then form the element stiffness matrix in a straightforward manner. Numerical integration along the length was used. Assembling the six resulting stiffness matrices we obtain the 63 by 63 stiffness matrix for the hexagonal prism. The stress field in the subelement is constant in each triangle and will vary linearly along the length.

The finite element analysis described above for the hexagonal prism has been incorporated into a computer program. The analysis and program have been tested using the four St. Venant problems (extension, torsion, pure bending, bending with shear) as comparisons — these problems have well-known exact or engineering solutions. The loading conditions and results are given in Table V. Three integration points were used along the length of the element, and isotropic properties were taken with a modulus of 1×10^6 MPa and Poisson's ratio of zero.

We have concluded from the results of this study that the prismatic finite element described here is adequate to represent the three-dimensional structural behavior of graphite core blocks, and when incorporated into HTGR core models, would lead to major improvements in predicting the dynamic response of core block assemblages to seismic excitation.

5. Simulated Earthquakes

Horizontal and vertical time histories of the General Atomic 0.5 g simulated earthquake have been received. Response spectra for these time histories have been generated, and they compare favorably with those published in the GASSAR. These time histories will be used to excite our one- and two-dimensional core seismic models.

C. Preliminary Study of HTGR Core Support Post Stability (C. A. Anderson)

In the large HTGR designs the core is supported on an arrangement of graphite support posts, and questions have been raised as to the long-term stability of this core support method taking into account graphite material property degradation caused by irradiation and a moisture environment together with the potential for seismic excitation. The purpose of this investigation is to assess the probability of core support post instability under these conditions. We will employ a deterministic mechanical model of the core and its support post together with some classical methods of reliability analysis as applied to earthquake engineering in order to carry out the analysis.

Figure 27 illustrates the support post model which will be used in this investigation; $\ddot{u}_o(t)$ and $\ddot{v}_o(t)$ are the base vertical and horizontal accelerations. The initial studies will be concerned only with the elastic, large deflection

TABLE V

COMPARISON OF NUMERICAL AND EXACT RESULTS FOR PRISMATIC FINITE ELEMENT UNDER ST. VERNANT LOADING SITUATIONS

Problem	Loading Condition	Length	Theoretical Displacement or Angle of Twist Per Unit Length	Finite Element Displacement or Angle of Twist per unit Length	Theoretical Stresses	Finite Element Stresses
Uniform Extension	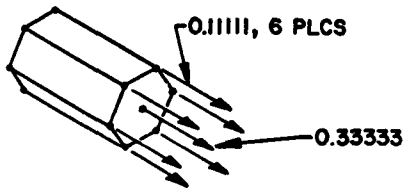	$\frac{2}{1}$	3.079×10^{-11}	3.079×10^{-11}	1.54	1.54
Pure Torsion	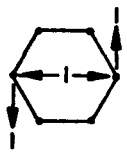	$\frac{2}{1}$	3.094×10^{-10}	4.076×10^{-10}	5.81	5.38
Pure Bending	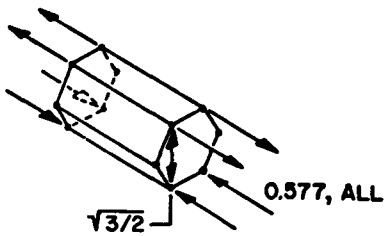	$\frac{2}{1}$	1.477×10^{-10}	1.847×10^{-10}	8.51	10.67
Bending with Shear	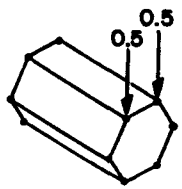	$\frac{10}{1}$	9.85×10^{-8}	9.41×10^{-8}	66.17	55.29

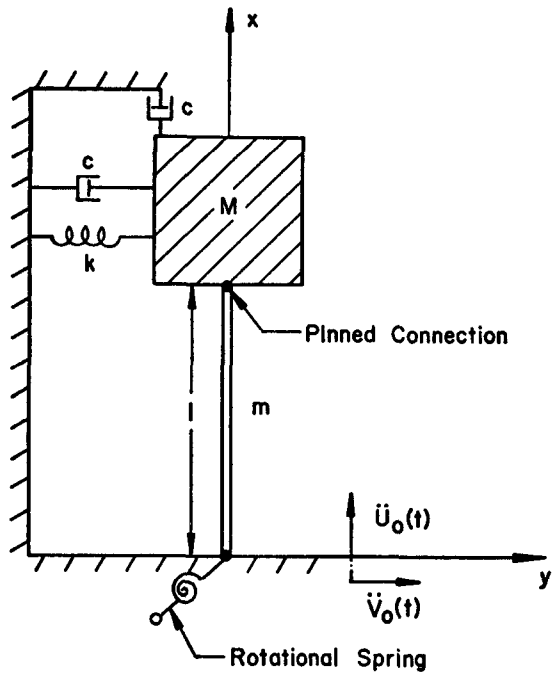

Fig. 27. Core support post model.

behavior of the core support post; later studies may include inelastic material behavior of the post. Typically the nominal post dimensions are 2 m in length and 150 mm in diameter. The average stress acting in the post due to the dead load of the core is 3 MPa (420 psi) which corresponds to a factor of 5 to 20 less than the critical buckling load P_{cr}, depending on the column fixity conditions and elastic modulus used for the graphite.

Simple models for the behavior of end loaded columns have been investigated previously in the literature.[14,15] It has been shown that the behavior of a single degree of freedom model could be described by the ordinary differential equation

$$\ddot{v} + (\frac{c}{M})\dot{v} + \Omega^2[1 - \frac{P(t)}{P_{cr}}]v = \ddot{v}_o(t) \qquad (4)$$

where P(t) is the total axial loading on the column (dead load plus the vertical acceleration times the supported mass), Ω is the natural frequency of the system, P_{cr} is the critical buckling load, and v is the lateral deflection. From Eq. (4) we see that the apparent natural frequency of the system is dependent on P(t). In Ref. 15, Eq. (4) was solved for a particular band limited white noise simulated earthquake and results for various column length-to-diameter ratios were tabulated.

An adequate core support post model would be more complex than the structural models treated in Refs. 14 and 15. Besides being complicated by the large number of support posts and consequently a large number of degrees of freedom, the problem is further complicated by frictional effects between the support core masses and uncertain end conditions for each post. Although the model shown in Fig. 25 represents the behavior of only a single post and its supported mass, it does allow for elastic and frictional coupling between the supported mass and ground as well as the presence of flexible coupling of the post to ground. Later models will have more support posts.

Our approach to this problem will be to use the finite element method to describe the motion of the column and its supported mass under both vertical and horizontal earthquake motions $\ddot{u}_o(t)$ and $\ddot{v}_o(t)$, specified as time histories. Derivation of stiffness matrices for analyzing large deflection and stability of beam columns has been carried out following the work presented in Ref. 16. The equations of motion resulting will be integrated using Newmark's method. The time history of earthquakes will be obtained by using the SIMEAR[17] code for generating simulated earthquakes. Peak responses will be tabulated for column stiffnesses which take account of the degradation of material properties.

D. Code Development for Analysis of PCRVs (P. D. Smith and W. A. Cook)

The NONSAP nonlinear finite element code is being modified for analysis of three-dimensional models of reactor structures. As obtained from the University of California at Berkeley,the NONSAP code permitted three-dimensional analysis of dynamic problems which respond with large strains. Material models for three-dimensional analysis were limited to linear elastic, nonlinear behavior described with a piece-wise linear curve, and an elastic-plastic behavior following the Von Mises model.

Several modifications of the NONSAP code are underway to render it useful for analysis of the PCRV.

A subroutine has been added which permits specification of pressure loads on selected element faces. These pressure loads are transformed into a set of consistent nodal forces by use of the element shape functions.

A reinforced concrete model developed by Agbabian Associates[18] has been obtained from the Air Force Weapons Laboratory. The model computes a composite constitutive relation based on concrete and steel properties. The concrete is permitted to crack normal to principal stress directions. After cracks occur, bond degradation between concrete and steel is accounted for. Also, the enhancement of shear strength by dowel action across cracks is modeled. Currently the model is being debugged by applying uniaxial loads to a single three-dimensional element. An error in the formulation of the composite shear moduli has been found to be the cause of erroneous displacements observed for this test problem, and this situation has been corrected.

The single greatest limitation placed on three-dimensional analysis by the current version of NONSAP is its in-core solution algorithm. The maximum possible in-core solution using the CDC-7600 is limited to a stiffness matrix of 240 000 words. A minimal meaningful PCRV analysis might consist of 2000 degrees of freedom and a stiffness matrix bandwidth of 500. Such a problem exceeds CDC 7600 large-core memory capacity by a factor of four. A means of using an out-of-core equation solver is currently being investigated.

Figures 28 and 29 show a ring structure and a reinforced concrete beam which have been chosen as demonstration problems for NONSAP. These structures are also being used to validate the concrete model. Experimental data exist for the dynamically loaded beam test problem. In the future the ring will be used to demonstrate PCRV liner models and the beam will be modified to include prestressing tendons.

Future modifications to the NONSAP code will permit it to model thermal stresses and creep effects in three-dimensional structures. In addition, a

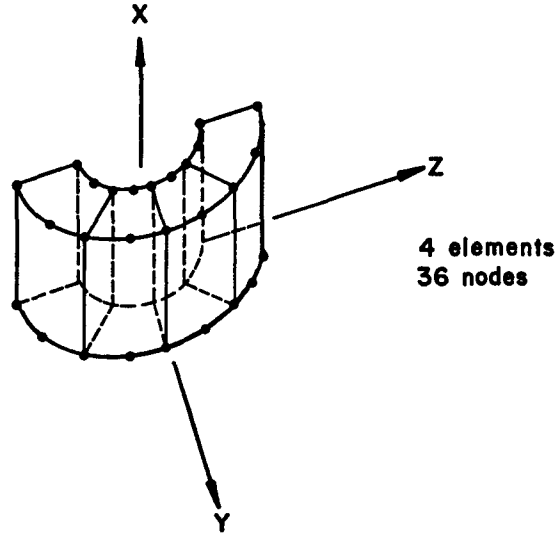

Fig. 28. Ring structure for NONSAP concrete test problems.

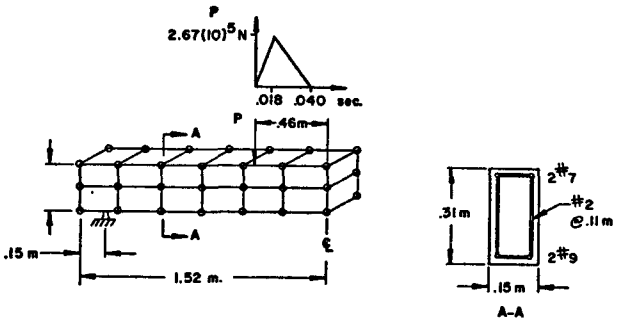

Fig. 29. Reinforced concrete beam model.

mesh generator and a graphics package for mesh plotting and output visualization will be added. Refinements of the concrete model are planned to more accurately represent concrete behavior under a tri-axial stress state.

VI. TASK 6, SAFETY INSTRUMENTATION AND CONTROL SYSTEMS

Efforts within this task area are directed to the assurance of the suitability and reliability of instrumentation and control systems used in HTGRs to monitor and control safety-related plant parameters during all modes of operation. Measurement of parameters which are significant to HTGR safety related research tasks is also being considered.

Instrumentation considered in this task area includes primary coolant moisture monitoring, temperature measurements, and neutron fluence measurements.

A. Primary Coolant Moisture and Impurities Monitoring (E. J. Dowdy)

Determination of the LASL Helium Afterglow Impurities Monitor* sensitivity for detecting primary coolant impurities other than moisture and competition among the impurity gas molecules for the available helium metastable atoms is awaiting completion of the fabrication of standard gas volumes. Accurate moisture content measurements over the range 0.2 to 2000 ppmV have been previously confirmed.

B. Temperature Measurements (V.Starkovich and B. Washburn)

Published information [19,20] on kryptonate properties and their application for maximum temperature determinations has stimulated consideration of the possibility that similar properties might be exhibited by HTGR fuel materials. The radioactive isotope ^{85}Kr has been diffused into graphites and solids having the graphite structure and stabilized.[19,20] These solid sources, termed "kryptonates", are subjected to a thermal environment where the maximum temperature is to be determined. Following this exposure, the solid source is thermally annealed and the krypton release or retention is measured as a function of time and annealing temperature. Annealing releases or release rates, which are different below and above the unknown thermal environment temperature, are interpreted as a function of annealing temperature to provide indication of the maximum temperature. Should fuel materials behave similarly to kryptonates with respect to detectable releases of krypton or xenon during post-irradiation thermal anneals, it may be feasible to passively determine HTGR maximum fuel temperatures attained during reactor operation. The annealing property of interest in crushed fuel beads is a detectable change in noble gas release or release at an annealing temperature corresponding to the irradiation maximum temperature.

Considerations, including discussions among the various task groups, outside consultation[21-27] and literature searches, have identified, but not satisfactorily resolved several important questions. Included are(a) the physics of the trapping and release mechanisms,(b) the trapping and release efficiencies, that is, the fraction of the total generated krypton or xenon atoms that would exhibit the desired

*For a discussion of the device and previous test results, refer to earlier quarterly progress reports: LA-5870-PR (2/75), LA-5975-PR (6/75), and LA-6054-PR (9/75).

temperature dependent trapping-release behavior, (c) the time dependence of the release, and (d) the most cost-effective means of performing an overall proof-of-principle experiment. Progress and status on these questions follow.

1. Trapping and Release Mechanisms

The literature reviewed has included publications on kryptonates,[19,20] reports on fission product release from reactor fuels and materials during post-irradiation thermal anneals[28-33] and reports on the behavior of related material physical properties during post-irradiation thermal annealing.[31, 34-38] The concept and terminology of trapping has been applied to describe the thermal annealing behavior of both kryptonates[20] and fission product release from reactor fuels.[39] The current limited understanding of the physics of the trapping-release phenomena is based on empirical methods and it is not clear at this time that the trapping-release mechanisms are the same in kryptonates as in reactor fuels. These mechanisms have not been quantitatively related to physical properties of the materials involved.

While limited knowledge precludes analogies between the observed trapping-release behavior in kryptonates and fuels, potentially important differences have been identified. Among these, kryptonated materials used for various measurements applications were subjected to certain treatments, during and following preparation and prior to measurement application, which are believed to affect the trapping, release, and stability.[19] It would not be possible to apply material quenching and initial degassing should these treatments be important to the trapping-release behavior of reactor fuel. We also have no information on the effect of irradiation upon trapping-release in kryptonates or fuels.

Calculations[39] of diffusion, assuming that atoms may be trapped and thus delayed in time from further diffusion, have shown good agreement with experiment for diffusion of rare-gas fission products from UO_2. This model gives two terms for diffusion from a sphere; one term reflects the quantity of atoms versus time leaked out from the original inventory in the matrix and the other term reflects corresponding leakage from the traps. The leakage from traps is generally slow and leakage from the matrix is fast. For three examples of experimental data[39] on diffusion from UO_2, calculations indicate that over 90% of the available atoms are trapped initially and that approximately 10^5 s elapse at annealing temperatures of 1300 and 1700°C before the xenon gas quantity released from traps equals that released from the matrix.

Pressures and temperatures used in the preparation of kryptonates by the diffusion method and those expected inside the HTGR fuel beads are comparable.

2. Trapping and Release Efficiencies

The review of data on fission product release from reactor fuels,[28-32] including crushed PyC coated beads,[25,26,33] during post irradiation thermal anneals has not suggested specific trapping-release mechanisms or quantities of fission products that might be expected from release from traps. Using existing diffusion data[30] and assuming a 10^3 s observation period with a release of 10% of the desired atoms, it is estimated that a trapping efficiency of approximately 10^{-3} is needed for a signal-to-noise ratio of one.

3. Release Time-dependence

No information has been found which confidently and directly reflects the desired trapping release time-dependence. In low temperature (400-1200°C) anneals of UO_2 and graphites,[30] typical two-step xenon diffusion rate curves are obtained. The fast portion lasts for 20-30 min and is followed by diffusion at a much slower rate. High temperature

(1400-2200°C) anneals of UC_2 with PyC coatings[29] and of sintered UO_2 (see Ref. 21) behaved similarly with respect to xenon release. There are at least two important rate-controlling processes.[28] The simplest of these processes (diffusion from cracks and pores) can be roughly approximated by an exponential decay law and the more complicated process (diffusion from grains) can be empirically described as the sum of two exponential terms as though it consisted of a fast and a slow process.

Available information on the annealing behavior of kryptonates[20] indicates similar two-step diffusion of krypton with the initial fast portion lasting approximately 20-25 min.

Interpretation of the model of Hurst[39] indicates that the atoms associated with trapping may make a very small (1% or less) contribution to the annealing release at early times, that is, during the fast release rate process, when the fraction of total atoms which are trapped may be high. The model allows for an atom to be trapped and released many times before eventually escaping and thus the time spent in traps may be much longer than the lifetime in a single trap. The contribution to the release from trapped atoms will lag that from the matrix by the mean lifetime in the traps.

These observations on releases and release rates indicate that at a given annealing temperature, releases would have to be monitored for periods greater than 30 min to detect effects of atoms escaping from traps. These observations should continue for approximately two hours in order to define the characteristics of both the fast and slow steps of the release, to establish possible existence of the desired behavior and to permit development of data interpretation techniques. Application of the technique may not require observations for periods significantly greater than 30 min. Additionally, a number (10-15) of annealing temperature steps below and above the irradiation temperature will be required to establish the temperature dependent behavior of the release and release rate.

4. Proof-of-Principle Experiment

Work is continuing to better assess potential approaches for quickly and effectively determining if irradiation temperature dependent noble gas trapping and release exist in HTGR fuel. Plans under consideration include coordination of this work with that which may be programmed by the fission product transport task and cooperation with other laboratories which are equipped to perform the necessary work.

5. Other Techniques for Maximum Core Temperature Determination

A preliminary review of maximum temperature determination by temperature-dependent release of fission products and by temperature-irradiation induced changes in material properties has been conducted. The main purpose, at this time, in reviewing information related to these techniques has been the search for indications of temperature-irradiation induced changes in material properties which might associate with mechanisms of noble gas trapping and annealing release.

Additional information will be reviewed and compiled for evaluation at a later time.

VII. TASK 7, ACCIDENT DELINEATION

(John E. Foley)

A. Introduction

The various factors that must be determined in order to estimate the risk to the population from the release of radioactive material during an accident at a nuclear power plant as given in WASH-1400 (Draft)[40] as:

1. the probability and magnitude of release of radioactivity,

2. the likelihood and characteristics of various meteorological conditions, and
3. the distribution of population that can be affected by the accident.

Of the above, only the "magnitude of release of radioactivity" is of concern to us at the present time in this task area. Because of this, "risk" is not the proper term to use for the consequences of our analyses because an estimate of "risk" requires that both the meteorological conditions and population distributions must be known in addition to the probability and magnitude of release of radioactivity. We will thus use a more limited definition of consequences of an accident by defining consequences to be simply estimates of the mean values and variances of the release rates of the isotopes of biological significance from the containment building to the environment. For the present, we plan on limiting our studies to potential accidents involving the reactor core. We will leave the analyses of potential accidents not involving the core (such as fuel storage accidents) to a later time.

At the present time, it is not clear how "plant specific" we should be in our analyses of the faults that initiate accidents. Since each HTGR plant is designed differently (by different architect-engineers), it will be difficult to define unique fault sequences leading to an accident. We feel that the accident delineation task should deal with "generic" HTGR problems, rather than with plant specific problems. Our initial emphasis will thus be placed on describing the sequences and on calculating the consequences following the postulated accidents; that is, we will emphasize the accident progression and consequence analyses rather than emphasize the initiating fault sequences. Many accidents are "generic" to the HTGR (such as depressurization, reheater leak, etc.) and the progression and consequence of these accidents can be described somewhat independently of the particular plant design. The cause, or initiating fault, of such potential accidents, however, may be quite specific. A flow diagram of the activities of this task is shown in Fig. 30. Our initial activities, as detailed above, will concentrate on the right hand portion of the figure.

The types of initiating phenomena that lead to potential accidents are: 1) core power/flow imbalances, and 2) loss of pressure boundary integrity. These phenomena can be further subdivided into:

1. Core power/flow imbalances
   a. Power transients
   b. Loss of circulation
2. Loss of pressure boundary integrity
   a. between primary coolant and containment building
   b. between primary and secondary coolant
   c. between primary coolant and auxiliary coolant

Event trees describing the progression of potential accidents will be developed in order to estimate the consequences of the various sequences. For a depressurization accident (case 2a above) the

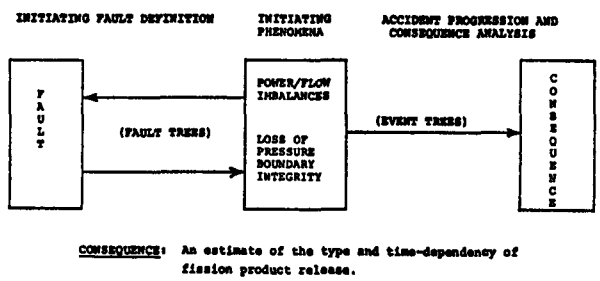

Fig. 30. Flow diagram of the activities of the accident delineation task.

consequences will depend on whether the depressurization is slow or rapid (because of lift-off of plated-out activity) and on whether various engineered safety functions (such as the containment cleanup system) work properly.

As we develop various analytical capabilities, we will begin to calculate the consequences of selected accident sequences defined by the event trees using the best available data. As we do this, the weak links in the analyses will become apparent. We will then have a better understanding of both the analytical and experimental areas that need additional work so that we can provide an independent evaluation of the consequences of the various accidents.

B. Simple Example

1. Containment Model

An example of the approach used in the analyses can be given by a simplified, but realistic, event tree for the containment building. This tree (Fig. 31) can be used for potential accidents such as a depressurization accident (initiating phenomenon 2a). The analysis of the consequences (mean value for this example) of the depressurization can be done in the following manner:

Assume that C_o curies of an isotope are released to the containment building at the onset of the depressurization. The time-dependent amount of the isotope C(t) in the containment building is then given by

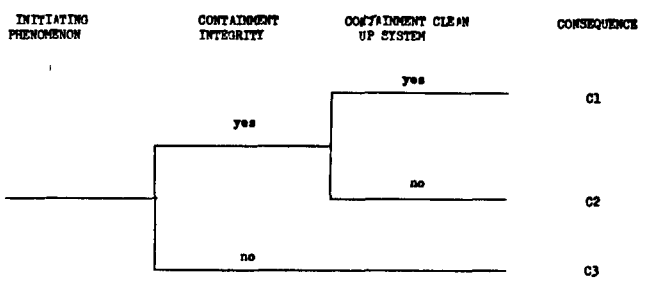

Fig. 31. Containment building event tree.

$$C(t) = C_o e^{-(\lambda + V + L)t} \quad (5)$$

where

λ is the radioactive decay constant of the isotope,

V is the containment cleanup system removal rate,

L is the containment building leak rate.

These three parameters (λ, V, L) will be considered to be constants during the entire period of the accident.

The leakage rate $\ell(t)$ of the isotope from the containment building is then given by

$$\ell(t) = L\, C(t). \quad (6)$$

The total amount L_t of leakage of the isotope from the containment building into the environment (that is, the consequences of the accident) is given by

$$L_t = \int_0^\infty LC(t)\, dt \quad (7)$$

$$= LC_o \int_0^\infty e^{-(\lambda + V + L)t} dt \quad (8)$$

$$= \left(\frac{L}{\lambda + V + L}\right) C_o . \quad (9)$$

The fraction F of the initial amount of the isotope that gets into the environment is then

$$F = \frac{L_t}{C_o} \quad (10)$$

$$= \frac{L}{\lambda + V + L} \quad (11)$$

This remarkably simple expression describes the relative consequences (mean value) of an accident with subsequent success or

failure of the containment cleanup system or the containment building.

2. Relative Consequences

For a numerical example, we will consider the release of ^{131}I. The values of the parameters[6] (for successful operation) in Eq. (11) are then

$$L = 4.17 \times 10^{-5}\ h^{-1}$$

$$V = 0.9\ h^{-1}$$

$$\lambda = 3.58 \times 10^{-3}\ h^{-1}\ .$$

If both the containment building and the containment cleanup system operate properly, the fraction of the ^{131}I released into the containment building that eventually gets into the environment is given by

$$F = \frac{L}{\lambda + V + L} = 4.62 \times 10^{-5}. \qquad (12)$$

This is the relative consequences of C1 in Fig. 31.

If the containment building operates properly, but the containment cleanup system fails (V = 0), then the fractional release of ^{131}I is

$$F = \frac{L}{\lambda + L} = 1.15 \times 10^{-2}\ . \qquad (13)$$

This is the relative consequences of C2 in Fig. 31.

If the containment building fails, then the fractional release of ^{131}I is simply

$$F = 1\ . \qquad (14)$$

In this case, it is immaterial whether the containment clean up system operates. The consequence C3 is thus unity.

3. Conclusions

Successful operation of both the containment cleanup system and the containment building reduces the mean value of the consequences of ^{131}I by a factor of 4.62×10^{-5} over that of failure of the containment building. Failure of only the containment cleanup system reduces the consequences by a factor of 1.15×10^{-2} over that of failure of the containment building.

VIII. TASK 9, PHENOMENA MODELING AND SYSTEMS ANALYSIS

A. Double-Heterogeneity Treatments Used for Generating HTGR Space-Shielded Cross Sections (M. G. Stamatelatos and R. J. LaBauve)

1. Introduction

The previously reported[41] route for generating cross sections for HTGR safety research at LASL used modified versions of the MC^2-I (Ref. 42) and GLEN (Ref. 43) codes together with TOR (Ref. 44) and HEXSCAT (Ref. 45) for graphite. Cross sections generated with these codes did not take into account the space shielding effects of the doubly-heterogeneous structure of the fuel-moderator system in an HTGR. In order to account for these self-shielding effects, as well as to better account for energy self-shielding effects due to large concentrations of heavy adsorbers in the fuel, an alternate route has been adopted. This route uses MINX,[46] a modern code under development at LASL, together with a modified version of the 1DX[47] code adapted to handle the Bondarenko energy self-shielding formalism provided by MINX in the above-thermal region. The thermal region cross sections are still being generated with a modified version of the GLEN code.

The new procedure is as follows:

a) Run MINX to generate point-wise (PENDF) cross sections in the ENDF format for the entire energy region.

b) Run the PETOPES[48] program to particle (grain) self-shield the PENDF cross sections for important heavy absorbers (that is, ^{232}Th, ^{235}U) in the entire region (14-0 MeV).

c) Use MINX to collapse the PENDF cross sections to two fine-group

energy structures, one in the above-thermal region (14 MeV-0.414 eV) and the other in the thermal region (2.38 eV - 0 eV). These cross sections are already grain shielded.

d) In the above-thermal region, run 1DX to collapse the fine-group cross sections to a broad-group structure. Gross heterogeneity (pin/moderator) corrections on the absorber cross sections are applied at this stage.

e) In the thermal region, run GLEN to calculate a thermal flux and to collapse the MINX thermal fine-group grain-shielded cross sections to a broad-group structure.

f) Format the broad-group cross sections in DTF style.

For various temperatures, only steps (c) through (f) need be repeated.

2. Grain Shielding Treatment

The grain shielding procedure adopted is that used by Wälti[49] which is apparently being used in the General Atomic code MICROX.[50] This procedure was claimed by Wälti to agree very well with the detailed Nordheim integral transport treatment used in GAROL[51] and in the GGC-5 code[52] which contains GAROL.

In the Wälti procedure, the grain-shielded absorber microscopic cross section is given by

$$\sigma_i^{eff}(E) = \sigma_i(E)\,\frac{\Gamma(E)}{1-r^3\,[1-\Gamma(E)]} \qquad (15)$$

where $\sigma_i(E)$ = unshielded cross section for the i-th heavy nuclide,

r = ratio of fuel to moderator radii in a two-concentric-sphere model (inner = fuel; outer = moderator) representing a uniform grain distribution in the fuel rod, and

$\Gamma(E)$ = self-shielding factor, that is, the ratio of average neutron fluxes in the grain and in the moderator, $\bar{\phi}_o/\bar{\phi}_1$, where subscripts o and 1 refer to the grain and the surrounding moderator regions respectively.

If isotropic augular fluxes are assumed for regions o and 1, the neutron balance equations for the two regions yield

$$\Gamma(E) \equiv \frac{\bar{\phi}_o}{\bar{\phi}_1} = \frac{1 + \rho\, Q[1 + W\bar{\ell}_1(\Sigma_{a,1} + \Sigma_{out,1})]}{1 + \rho\, Q + W\bar{\ell}_o(\Sigma_{a,o} + \Sigma_{out,o})} \qquad (16)$$

where

$\rho = \dfrac{\bar{\ell}_o}{\bar{\ell}_1} = \dfrac{V_o}{V_1}$ = volume ratio of regions o and 1,

Q = ratio of spacially averaged source densities in regions o and 1

$$W = 1 + \tilde{H}_o(\Sigma_{t,o}) + \tilde{H}_1(\Sigma_{t,1}), \qquad (17)$$

$\bar{\ell}_o$ and $\bar{\ell}_1$ are the mean chord lengths respectively:

$$\bar{\ell}_j = \frac{4V_j}{S_j}, \quad j = o,1 \qquad (18)$$

$\tilde{H}_j$ = first-collision "augment" for region j:

$$\tilde{H}_j(\Sigma_{t,j}) = \frac{1 - \tilde{P}_j}{\bar{\ell}_j\,\tilde{P}_j\,\Sigma_{t,j}}, \quad j = o,1, \qquad (19)$$

$\Sigma_{a,j}$, $\Sigma_{t,j}$ are the macroscopic absorption, out-scatter and total cross sections, respectively, for region j (o or 1).

$\tilde{H}_1(\Sigma_t)$ is approximated by $\tilde{H}_1(0)$:

$$\tilde{H}_1(0) = \left(\frac{\gamma}{2}\right)^2 \left\{ \left(1-r^2\right)^2 \left(1 + \frac{1}{4} \ell n \frac{1+r}{1-r}\right) - \frac{r}{2} \left(1-r\right)^2 + \left(\frac{2}{3r}\right)^2 \left[\left(1-r^2\right)^3 - 3\left(1-r^3\right)^2 + 2\left(1-r^3\right) \left(1-r^2\right)^{3/2} \right] \right\} . \quad (20)$$

where $\gamma = \dfrac{3r^2}{4(1-r^3)}$. (21)

$\tilde{P}_o$ is given by the expression[53]

$$\tilde{P}_o \left(\Sigma_{t,o}\right) = \frac{3}{8X^3} \left[2X^2-1 + (1+2X) \exp (-2X)\right] \quad (22)$$

where $X = \frac{3}{4} \bar{\ell}_o \Sigma_{t,o}$. (23)

Q is given by

$$Q = \frac{\xi_{o,pot} \Sigma_{s,o}^{pot}}{\xi_{1,pot} \Sigma_{s,1}^{pot}} \quad (24)$$

and the self-scattering cross section is approximated by

$$\Sigma_{ss,j}(E) \tilde{=} \frac{1 - \xi_j(E)}{\xi_1^{pot}} \Sigma_{s,j}(E) \quad (25)$$

where the average logarithmic energy decrement $\xi_j(E)$ is given by

$$\xi_j(E) = \frac{\sum_i \xi_j^i \Sigma_{s,j}^i(E)}{\Sigma_{s,j}(E)} \quad (26)$$

i being the nuclide index.

Derivation of these expressions and justifications of the approximations used can be found in Ref. 49.

A special computer program, PETOPES, was written in order to apply the above formalism to PENDF cross sections generated by MINX transforming them into grain-shielded PENDF cross sections for further processing by the MINX code.

Results of the PETOPES program agree very well with those published by Wälti[49] for the ThC_2 grain structure of the Fort St. Vrain (FSV) HTGR.

3. Fuel Pin Heterogeneity Treatment

The escape probability from a regular array of fuel (absorber) lumps, each assumed homogeneous in composition, is given by the usual expression

$$P_{esc}^* = P_{esc} \frac{1 - C}{1 - C \left(1 - \Sigma_F \bar{\ell}_F P_{esc}\right)} \quad (27)$$

where P_{esc} = escape probability from one lump,

C = Dancoff factor, and

$\bar{\ell}_F$ = fuel-rod mean chord length.

Expressions for P_{esc} for various lump geometries have been derived by many investigators (that is, see Refs. 53,54, and 55). Wigner[56] has proposed a "rational" approximation for P_{esc} which gives the correct value for very large or very small lumps. For better approximations

between the two extreme limits, various Wigner-like approximations have been proposed. One popular version is due to Levine:[57]

$$P_{esc} \approx \frac{1}{1 + \Sigma_F \bar{\ell}_F / A} \qquad (28)$$

where A = Levine factor (pin-geometry dependent).

For cylindrical pins, Otter[58] has found that the energy-independent value 1.35 for A works quite well for a large range of fuel-pin radii. If expression (28) is substituted into (27), it can be shown that P_{esc}^* can be written

$$P_{esc}^* = \frac{1}{1 + \Sigma_F / \Sigma_e} \qquad (29)$$

where the effective cross section Σ_e is given by

$$\text{cross } \Sigma_e = \frac{(L - C)\, A}{\bar{\ell}_F \,[1 + C\,(A-1)]} \quad . \qquad (30)$$

The advantage of the rational form of Eq. (29) is the equivalence between the heterogeneous system and a homogenized system for which the moderator cross section is equal to the moderator cross section in the fuel pin of the heterogeneous system plus the effective cross section Σ_e.[59,60] This implies that pin heterogeneity corrections to cross sections can be made by simply adding Σ_e to the moderator cross section in the fuel and treating the system as homogeneous.

This formalism has been included in a modified version of the 1DX code.

4. Alternate Simplified Double-Heterogeneity Treatment

Preliminary calculations have shown successful results with a considerably simplified method for treating the double heterogeneity in HTGR fuel pins without first grain-shielding the cross sections at the PENDF level as discussed above. This method, an extention of the pin heterogeneity correction method, is designed to be used as a rapid independent check of the more elaborate method discussed above. Full details will be reported subsequently.

B. HTGR Neutronic Analysis (J. C. Vigil and P. G. Bailey)

We have completed drafting a report,[61] "Beginning-of-Life Neutronic Analysis of a 3000 MW(t) HTGR," which describes in detail the methods, models, and results of an independent study of safety-related neutronic characteristics for the BOL core of the FGS HTGR.

During the quarter, we have used perturbation theory to compute two-dimensional material worth distributions in the HTGR. We have also computed isothermal temperature coefficients for conditions which approximate those at the end of the equilibrium cycle (EOEC). These computations are described below.

1. Material Worth Distributions

We have used two-dimensional (R-Z) direct and adjoint angular fluxes for the unrodded BOL Fulton Generating Station (FGS) to compute small-sample worth distributions for various materials using perturbation theory. The materials for which worth distributions were computed, and their maximum specific worth, are given in Table VI. In general the location of the maximum worth is near the center of the reactor core.

Radial and axial worth distributions for representative materials are discussed below. In all cases we have shown the radial distribution at the axial mesh interval nearest the midheight of the core and the axial distribution at the first radial mesh interval. In the radial direction, the active core extends from 0 to 4.22 m and in the axial direction it extends from 1.19 to

TABLE VI

MAXIMUM REACTIVITY WORTHS
FOR VARIOUS MATERIALS

Material	Maximum Worth (¢/g)
Uranium - 235	$+ 1.34 \times 10^{-2}$
Uranium - 233	$+ 2.16 \times 10^{-2}$
Protactinium - 233	$- 1.13 \times 10^{-2}$
Thorium - 232	$- 6.25 \times 10^{-4}$
Xenon - 135	$- 1.65 \times 10^{2}$
Boron - Natural (unshielded)	$- 7.06 \times 10^{-1}$
Boron - Natural (shielded in burnable poison pin)	$- 4.74 \times 10^{-1}$
Boron - Natural (shielded in control rod)	$- 1.01 \times 10^{-2}$
Silicon - Natural	$- 5.46 \times 10^{-5}$
Carbon - 12	$+ 2.86 \times 10^{-5}$
Oxygen - 16	$+ 1.27 \times 10^{-5}$
Water (H_2O)	$+ 9.04 \times 10^{-4}$

7.53 m. Graphite reflectors completely surround the active core to yield overall dimensions of 5.25 m (R) and 8.72 m (Z) with the top boundary of the top reflector located at Z = 0.

Radial and axial worth distributions for ^{235}U are shown in Figs. 32 and 33, respectively. The reactivity worth for ^{235}U is positive everywhere and the worth curves generally reflect the thermal flux distribution. Peaking at the core-reflector interfaces is evident in both the radial and axial profiles. Radial zoning of the burnable poison depresses the radial thermal flux profile near the center of the core.

The radial and axial worth profiles for ^{233}U are very similar to those for ^{235}U, but the specific worth of ^{233}U is about 1.6 times higher than that for ^{235}U. In other words, the

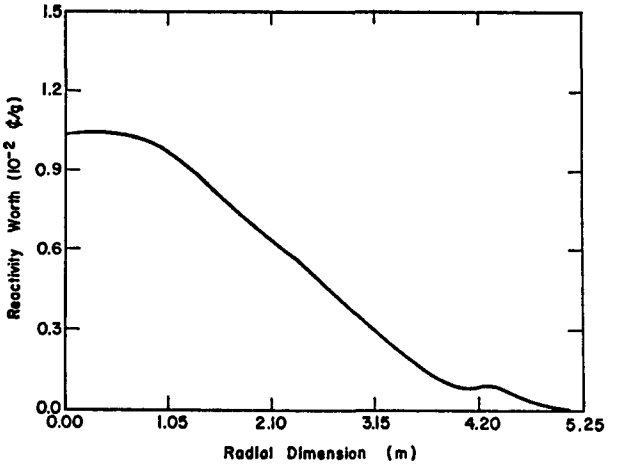

Fig. 32. Radial reactivity worth distribution for ^{235}U at Z = 4.3 m.

reactivity worth of 1.0 g of ^{233}U is equivalent to 1.6 g of ^{235}U. The specific worth of ^{233}Pa is negative, but of the same absolute magnitude as that for ^{235}U. However, ^{233}Pa decays to ^{233}U by beta emission with a 27 day half-life. Therefore, the maximum net reactivity change due to decay of ^{233}Pa is about $+3.29 \times 10^{-2}$ c/g or about 2.5 times higher than the value for ^{235}U.

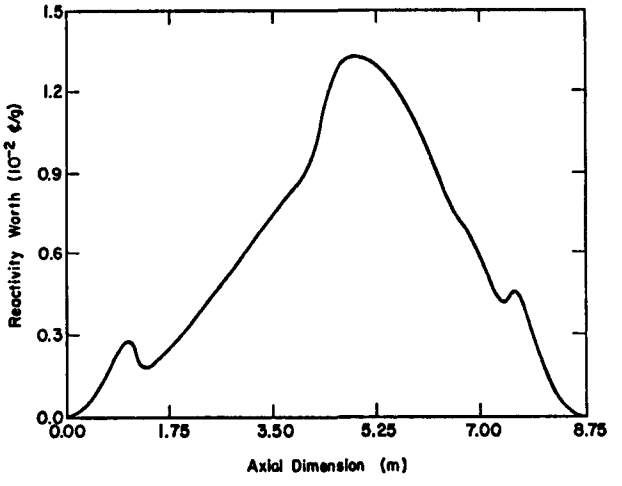

Fig. 33. Axial reactivity worth distribution for ^{235}U at R = 0.08 m.

Radial and axial worth profiles for ^{233}Pa are similar to those for ^{232}Th, which are shown in Figs. 34 and 35. Thorium has a negative specific worth whose magnitude is about twenty times smaller than that for ^{235}U. Because thorium is principally a resonance neutron absorber, the worth profiles reflect mostly the resonance neutron flux distribution which does not exhibit a reflector "bump."

The shapes of the ^{235}U worth curves (Figs. 32 and 33) are representative of all materials that are primarily thermal neutron absorbers. Thus, except for the sign, the curves for xenon, boron, and silicon are very similar to those for ^{235}U. On a unit mass basis, the reactivity effect of ^{135}Xe is about 230 times larger than that of unshielded natural boron. The reduction in the specific worth of boron in the burnable poison pins and in the control rods is consistent with the thermal flux shielding factors for these components.

In the HTGR, the reactivity effects of carbon, oxygen, and water are primarily due to neutron moderation.

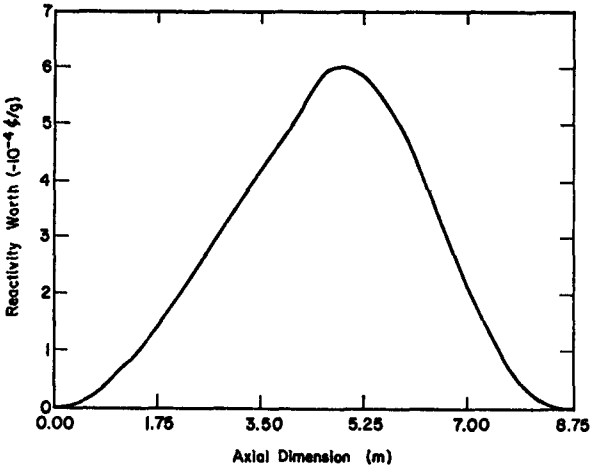

Fig. 35. Axial reactivity worth distribution for ^{232}Th at R = 0.08 m.

That is, these materials tend to soften the thermal neutron spectrum and this results in an increase in reactivity in the BOL core. Radial and axial worth distributions for water are shown in Figs. 36 and 37. Note that the worth of water becomes slightly negative in the reflector where absorption effects

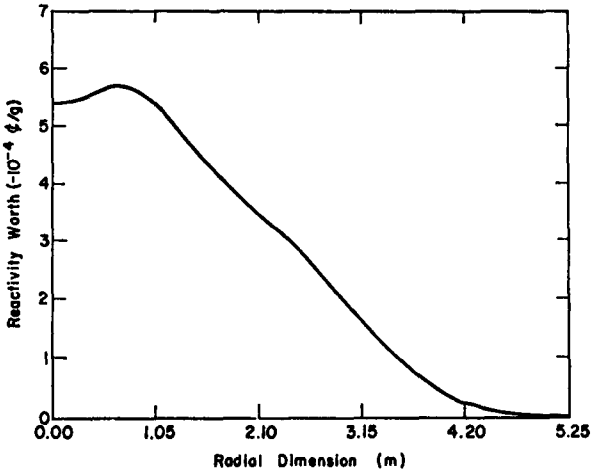

Fig. 34. Radial reactivity worth distribution for ^{232}Th at Z = 4.3 m.

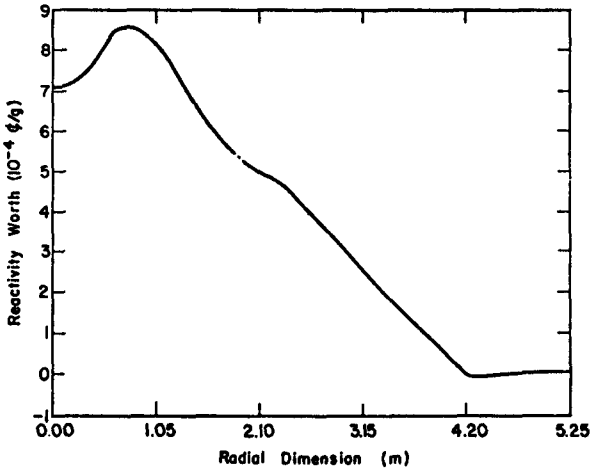

Fig. 36. Radial reactivity worth distribution for H_2O at Z = 4.3 m.

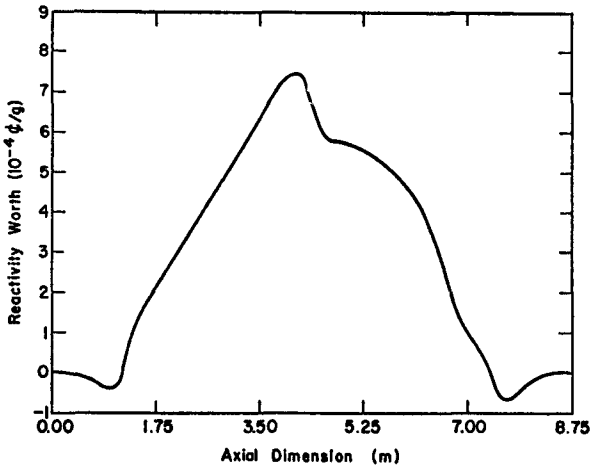

Fig. 37. Axial reactivity worth distribution for H_2O at R = 0.08 m.

become more important than moderation effects. The curves for ^{12}C and ^{16}O are similar to those for water except that the reactivity worth is positive everywhere.

Compared to carbon, the maximum specific worth of oxygen is two times smaller whereas that of water is about thirty times larger. These results reflect the relative efficiency of hydrogen, carbon, and oxygen as neutron moderators. Using the maximum specific worth for water, about 110 kg are required to yield a one dollar positive reactivity addition. The corresponding mass for carbon is about 3500 kg.

2. Preliminary EOEC Isothermal Temperature Coefficient Analyses

Previous studies of the FGS isothermal temperature coefficient have concentrated on the BOL reactor. Among these studies was one in which various fractions of the initial ^{235}U loading in the BOL core were replaced by ^{233}U (see Ref. 62). We found that replacement of ^{235}U with ^{233}U in the BOL core results in a less negative temperature coefficient and that the magnitude of the effect increases with both the ^{233}U fraction and with core temperature.

We have recently performed calculations for conditions which are more representative of the EOEC than in the previous study. The temperature coefficient of the EOEC core should include the effects of fuel burnup, conversion of ^{232}Th to ^{233}U, fission product and actinide buildup, burnable poison depletion, control rod withdrawal, and core neutron leakage.

The uranium and thorium atom densities used in the calculations are based on the EOEC loadings reported by the vendor.[2] As shown in Table VII, the EOEC fissile (^{235}U + ^{233}U) and ^{232}Th loadings are, respectively, about 83% and 86% of the BOL loadings. At the end of any given cycle, most of the burnable poison will have been depleted and, except for the central regulating rod pair, all control rods will have been withdrawn. Hence the effects of burnable poison and control rods were not included in our EOEC calculations.

TABLE VII

TOTAL CORE FUEL LOADINGS (KILOGRAMS)

Nuclide	BOL	EOEC
^{232}Th	37 487	32 238
^{235}U	1 617	746
^{233}U	0	593

Xenon and samarium are expected to be the most important fission products with respect to their effect on the temperature coefficient. Therefore, equilibrium concentrations of ^{135}Xe and ^{149}Sm were included explicitly. Other fission product poisons were represented by a 1/v poison (unshielded boron) whose concentration in the core was adjusted to yield a multiplication factor of unity at 1200 K.

Radial neutron leakage from the core was taken into account explicitly in the one-dimensional (cylindrical), two-zone (core and reflector) geometric model. Axial leakage was included implicitly through the use of buckling absorption losses.

Microscopic cross sections were interpolated from a nine-group MICROX library for the EOEC fuel loadings and seven different isothermal (fuel and moderator) temperatures . Criticality calculations were performed with the DTF-IV (Ref. 63) transport theory code in the S_4 approximation.

Multiplication factors for the seven isothermal (core and reflector) temperatures are shown in Fig. 38. For comparison purposes, we have also shown the results obtained for the unpoisoned BOL core using the same geometric model. Temperature coefficients were calculated from the data in Fig. 38 by using quadratic polynomial fits to successive data points (three points at a time). The results, shown in Fig. 39, indicate that the EOEC coefficient becomes positive above 1900 K.

C. CHAP Code Development

1. CHAP Status Report (P.A. Secker and J. S. Gilbert)

Drafting of a report[64] that describes the development status of the Composite HTGR Analysis Program (CHAP) was completed and a copy of the draft was submitted to RSR. The report provides a description of the philosophy, structure, and capabilities of the CHAP code. Detailed descriptions of those component models which were complete by the end of FY-1975 are provided. Some auxiliary analysis codes which are used in component model validation and evaluation are also described in the report.

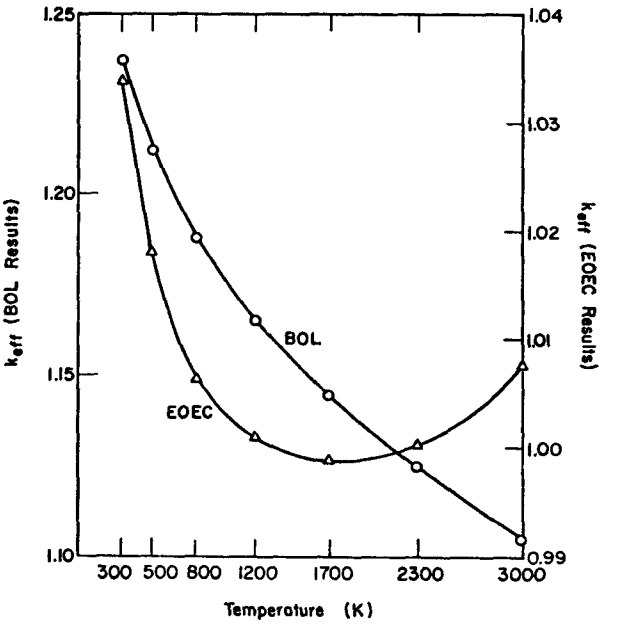

Fig. 38. Effect of temperature on the effective multiplication factor.

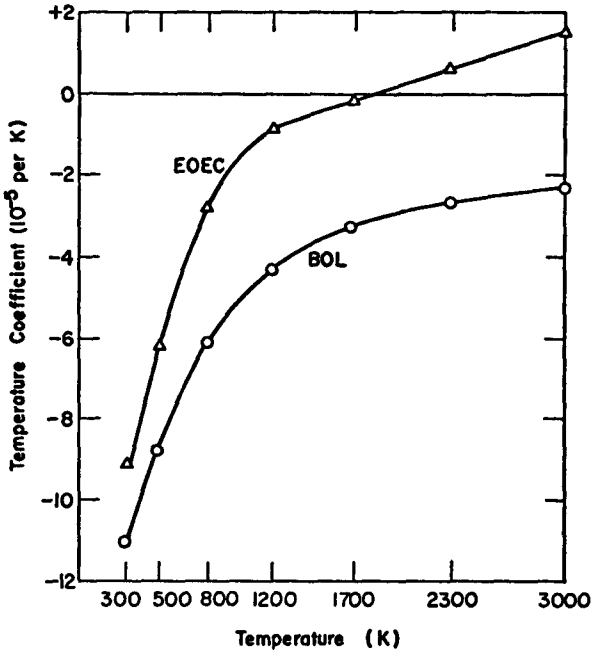

Fig. 39. Effect of temperature on the isothermal temperature coefficient of reactivity.

The report is intended as a status report and is not a user's manual for the CHAP code. Therefore, all information concerning the code structure is preliminary and is subject to change.

2. Conversion to a Modular System (P. A. Secker, M. J. Wecksung, and G. Willcutt)

The structure of the CHAP code has been extensively revised to accommodate a modular approach to component modeling. Conversion to modules of component models previously incorporated into CHAP is in progress. All new component models added to CHAP will conform to the modular concept.

In the modular approach, component models of varying mathematical complexity can be replaced easily by the user. This flexibility has many advantages. For some classes of problems the performance of a particular component may be critical to obtaining an accurate solution and vary detailed calculations of the model phenomena may be necessary. In other classes of problems only very crude calculations may be required. In still other classes the component response may not even be required. If the user had two or more validated models available he could use the model most appropriate for the class of problem being studied. In coding a component model, the only information required would be the appropriate model inputs and the coupling relationships between components.

Figure 40 is a block diagram of the revised CHAP program. Basically the CHAP main program performs input/output functions and transfers execution to appropriate subroutines for steady-state solution and/or transient response solution options which are user specified. CHAP is coded in standard FORTRAN-IV and follows closely the guidelines established for exportable reactor physics codes.[65]

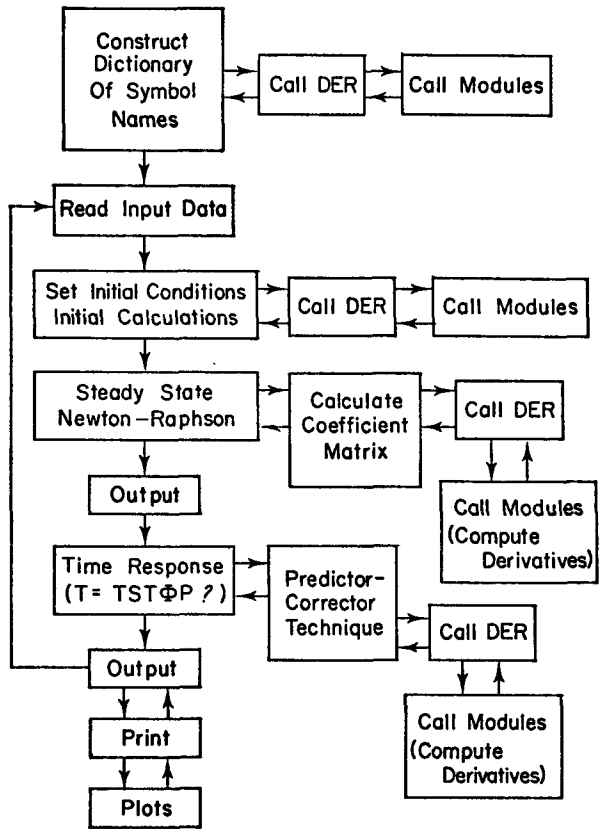

Fig. 40. Block diagram for CHAP.

CHAP uses a free format input package indentified as SYMPKG[66] which was written at LASL to be used primarily with codes that solve engineering problems. SYMPKG is a set of subroutines, written mainly in FORTRAN-IV, for use on the IBM 7094 and CDC 6000 and 7000 series computers. SYMPKG contains one assembly language subroutine called SYMBST, which consists of eight statements. This assembly language subroutine is the only departure from FORTRAN-IV in the CHAP program. However, it has been successfully converted for use on the IBM 7000 series, IBM 300 series, CDC 6000 and 7000 series, and UNIVAC computers. The SUMPKG routine is in common use by such companies as Westinghouse, Babcock and Wilcox, Aerojet, and Stone and Webster as well as many universities and research laboratories.

The steady state and time responses performed in CHAP are based on the solution of nonlinear simultaneous first-order ordinary differential equations. These system equations are defined in user written subroutines, called modules, which are called in proper sequence in a driver subroutine called DER. The modular approach permits easy updating of the composite model (subroutine DER) as more refined or better validated component models become available.

CHAP contains two different steady-state solution options and ten different numerical integration-technique options, two of which are implicit. However, defaults are provided so that the user need not be burdened with learning the details of each option. The default options provide for solutions with techniques that are both efficient and accurate and have been extensively tested.

We have developed a standardized module internal structure that is simple in concept and allows the user a great deal of freedom in programming. Each module subroutine is organized into three specific regions. Within the module module the user writes a FORTRAN computed GO TO statement which transfers execution to the appropriate region.

The component subroutine name is arbitrary, but the first four arguments of the subroutine are standardized. These arguments correspond to the module number, the number of state variables within the module, the address of the first state variable in the module, and the address of the derivative of that variable. For example, the call statement might appear as

```
CALL MOD1 (KM, NV, Y(NV+1), YP (NV+1),
ARG5, ..., ARGN).
```

The module number, KM, is updated by one within the module and the number of system state variables, NV, is updated by the number of state variables within the subroutine. The user is free to include COMMON blocks or additional subroutine arguments.

The computed GO TO statement must be included after KM and NV are updated to transfer execution within the subroutine. The first region is written by the user to set up a dictionary of external input/output names associated with variables used in coding the subroutine. A special subroutine, called BCDCON (BCD, A1, ..., AN), has been provided for this purpose. BCD is a dimensioned variable of Hollerith names which are associated with the coding variables A1 through AN.

Three other special subroutines are provided which are associated with BCDCON. They are CPLOT, CLIST and TITLE. Subroutine CPLOT (BCD) has an argument list of all module BCDCON names of variables which will be plotted during a time response calculation. Similarly subroutine CLIST (BCD) has an argument list of all BCDCON names of variables which will be listed. Subroutine TITLE (BCD) contains any desired title to be used for the module. Since the same component subroutine might be used more than once in a systems model (for example a model of a valve could be used extensively), the TITLE subroutine would identify the appropriate component. In this first region of the module a call to subroutine TITLE is always the last call and must be included. Within subroutine TITLE all module input/output names and plot and list variables are alphabetically arranged for main program use.

After the external input/output names are established the input data are read. The second region within a module is provided to perform problem initialization. All preliminary calculations and state variable initial condition calculations should be made in this region.

The third region within a module is used to compute the state variable derivative relationships, YP(I), when the state variables, Y(I), are provided. All associated algebraic calculations are also performed in this region. In essence the CHAP main program requires derivative values computed in the module subroutine in order to update the state variable values used by the module. The user is free to use any coding techniques he wishes and any variable names desired to construct the mathematical model.

We have provided special subroutines for parallel channel static flow balances and for tabular functions. Occasionally two or more components have parallel flow channels. A common block of flow rates, pressure drops, and total flow variables can be used in these modules so that the flow balances are externally computed. Tabular functions are used frequently in computation. Two subroutines called ENTER and ENTERP are provided which use linear interpolation to compute y as a function of x or x as a function of y given the x-y data array.

3. Component Model Validation (P. A. Secker and J. S. Gilbert)

Mathematical representations of component models are in terms of real physical variables. The equations contain physical descriptions of the thermal, fluid flow, neutronic, control, and safety-significant processes of each component. They are based on physical laws and component design and attempt to represent accurately both the static and dynamic characteristics of the component.

The degree to which the behavior of the system model represents that of the actual plant depends on the validity of the defining equations and various simplifying assumptions made in arriving at the model. These assumptions are based on an evaluation of the basic operation of the system components and how each component will influence the overall plant performance. Such items as the degree of coupling between dynamic modes and the frequency range of interest must be considered in arriving at these assumptions. Model validation of each component is important in order to demonstrate the correctness of the equations and assumptions.

If the component description results in a model which does not closely represent the physical behavior, the model is essentially of little value. However, undue complexity in model formulation must be avoided because computer running times, and consequently analysis cost, increase rapidly with the degree of complexity. The "best estimate" model, for the purposes of CHAP, is one that provides, with minimum mathematical complexity, all the information necessary to accurately satisfy the analysis for which the component model was intended. In the development of each component model, we attempt to minimize the number of state variables necessary to describe the component.

Ultimate verification of a reactor plant transient model requires comparison of the model results with plant transient data. Without this data, reasonable verification can still be obtained using two types of model comparisons. First, results from a simple state variable model for a component can be compared with results from a more detailed and complex solution to the basic partial differential conservation equations describing the component. For example, we have checked the average fuel and moderator temperatures from the relatively simple CHAP core model with those from a two-dimensional finite-element solution of the heat conduction equations. In a second kind of comparison, one possible state variable model

can be compared with another model which perhaps contains a larger number of state variables. During development of CHAP, we are comparing different state variable representations of certain components so that we can determine the simplest model which adequately represents the component response.

The dynamic response of a model can be examined in the time (t) or the frequency (ω) domain. In the time domain a specific disturbance is selected and the ordinary differential equations are numerically solved. To find the effects of other transient disturbances the equations must be solved again. The frequency domain can offer a significant advantage in representing component dynamics for model verification because a wide range of responses can be examined with a single computer calculation. The basic approach is to compare the same output variable response to a given input for several models of a component which have varying complexity. For example, a complex component model might include many spatial nodes for flow and thermal calculations, detailed descriptions of momentum, energy, and mass dynamic storage effects, sophisticated equation of state models, etc. A simplified model of the same component would contain fewer state variables by reducing the number of spatial nodes, neglecting certain dynamic storage effects, and using simple approximations for the equation of state models. Of course it might be possible to have many models of the same component which lie between the two versions. In general all component outputs affecting overall plant response should be examined with respect to all plant inputs to that component. Details of frequency domain transfer function analyses are presented in Ref. 64. Transfer functions for a model can be obtained for all possible combinations of model outputs with respect to any perturbed input. Physically meaningful selections, however, are based on inputs required by the component model and outputs required by other component models. A frequency response study is then performed for each transfer function at a specific operating level for the most detailed and complex model available. From this set of responses the dynamic frequency range of interest can be established. For example, when the input to a component is a sine wave with amplitude A and frequency ω, the output will also be a sine wave with the same frequency, but the amplitude may be different and the response may be shifted in time. At some input frequency, say ω_m, the output sine wave amplitude is attenuated by two to three orders of magnitude and remains below this amplitude for all $\omega > \omega_m$. We then establish that the frequency range of interest for this particular response is $0<\omega<\omega_m$.

We say that two component models are dynamically similar if the output sine wave amplitudes and phase shifts agree within acceptable error bounds over the frequency range of interest for each of the specified component transfer functions. By studying the frequency response at various steady state operating levels the nonlinear characteristics of the model can be determined. Consideration of the total operating range identifies the significance of nonlinear effects for a component model. If the frequency response of a specific component output with respect to a given input varies significantly at different operating levels, nonlinear characteristics are important. In these cases selected time response studies must also be made to ascertain that two different models of a component are dynamically similar. Final verification of the models comes when the transient and frequency response

characteristics of a component model are compared with actual test data for that component.

To this point we have discussed the validation of only one component model. Frequency domain transfer function techniques are applied to linearized model equations. The principal of superposition, therefore, can be utilized in order to discuss the validity of the dynamic response of composite models when the individually validated component models are coupled. If it has been determined that two separate components have mildly nonlinear characteristics it is reasonable to assume that the coupling of these two components will produce a composite transfer function nearly equivalent to the product of the two separate transfer functions. The key of course is the degree of nonlinearity. If the effects of component nonlinearities have been evaluated and included in each component model, and if all component models are dynamically valid within the same frequency bandwidth, we conclude that the coupled models will also be valid within that bandwidth.

4. Numerical Integration Techniques (P. A. Secker)

We have continued to evaluate numerical integration techniques for CHAP. In particular we were concerned with the ability to integrate the derivative equations associated with the steam generator model. These equations are highly nonlinear and represent moving boundaries over the evaporator length.

The method used to integrate the reactor core thermal equations in CHAP were reported previously.[62] This method was modified slightly and has been used successfully to solve a number of nonlinear test problems which are not well-posed in the large. One problem was the second-order Van der Pol's limit cycle with initial conditions such that the solution is stable and periodic. The basic equations are

$$\frac{d}{dt} y_1 = y_2 \qquad (31)$$

$$\frac{d}{dt} y_2 = 5(1 - y_1^2)y_2 - y_1 \, . \qquad (32)$$

Figures 41 and 42 show the numerical solutions to y_1 and y_2 as a function of time for two cycles and illustrate the stability of the method.

Another problem which was studied is outlined in Gear's[67] text. It is a fourth-order nonlinear set of "stiff" equations which has an analytic solution. The maximum relative error in any of the four state variables after 3 s of solution time was 3×10^{-5}. The local error criterion was 10^{-6}. The solution required 0.5 s of CDC machine time and involved 350 time steps with time step changes. The method compares very favorably with methods used by Gear.

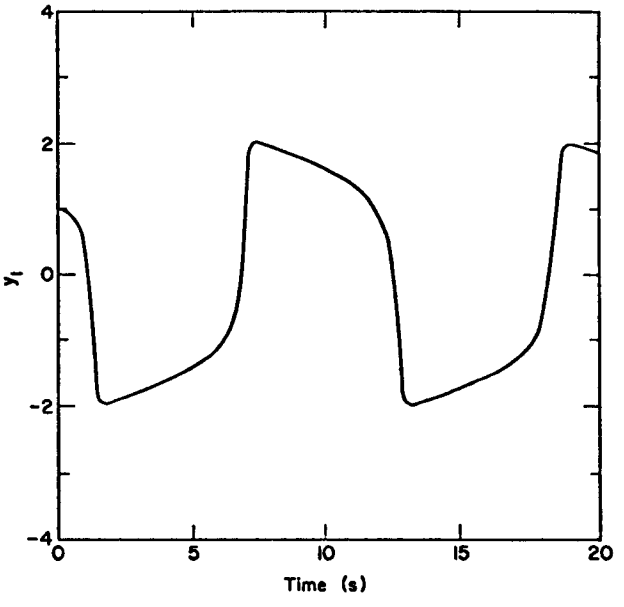

Fig. 41. Solution of y_1 in Van der Pol's equations.

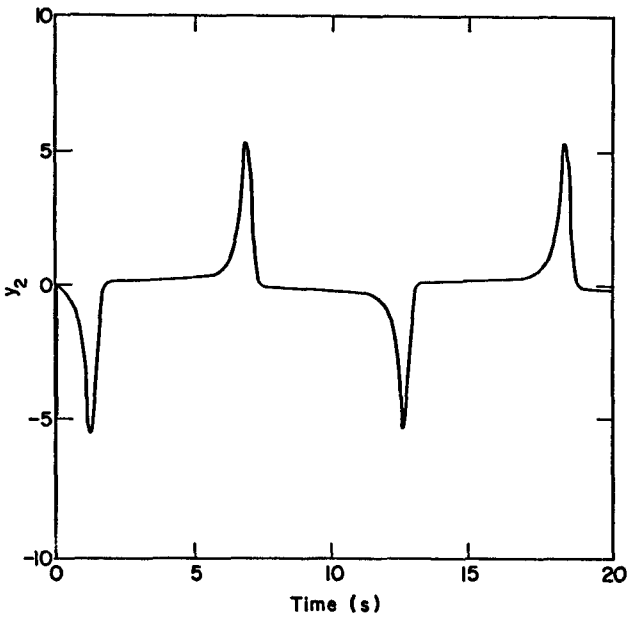

Fig. 42. Solution of y_2 in Van der Pol's equations.

Finally the technique was incorporated into the DARE[68] simulation program which was developed at the University of Arizone (UA). It was used to solve the nonlinear, moving-boundary, model of the Clinch River LMFBR steam generator developed by the UA Department of Nuclear Engineering. The method was found to be superior to other techniques used in the past with respect to computer running times. The accuracy of the method was also established.

With this background we are hopeful that the method will be adequate for the entire HTGR plant solution.

5. HTGR Loss-of-Forced Cooling Model (G. Willcutt)

A preliminary core model containing up to five channels has been developed and tested for a few time steps for complete loss-of-forced cooling. The model calculates natural convention flows in the channels and includes flow reversals so that the net core flow is zero.

Each channel represents a region of the core with one solid temperature node per axial block. Each region includes one node for the top reflector, eight active core nodes, one node for the replaceable bottom reflector, one node for the permanent bottom reflector, and one node for the core support block. Coolant nodes for each channel are located at the top, middle, and bottom of each solid block.

Temperatures of the solid nodes are calculated assuming there is no radial conduction between regions or axial conduction between blocks. Heat generated in the block is a function of the region peaking factor, axial peaking factor, and a decay heat equation. Heat removed from the block is equal to the heat gained by the coolant. For each time step, the energy balance between heat generated, heat lost to coolant, and change in energy of the block is used to calculate the new block enthalpy and a derived equation of enthalpy versus temperature is used to determine the block temperature.

Coolant temperatures are calculated assuming that the entire solid in a region is at a uniform temperature at each axial location and that the solid temperature varies linearly between solid nodes or is extrapolated linearly for the top and bottom nodes. Heat transfer coefficients are based on standard correlations.

The coolant flow distribution is calculated in a two step process. An outer loop estimates the core pressure drop needed to get no net flow (sum of up and down flows), and an inner loop calculates the flow in each channel to match the given core pressure drop. An improved estimate of the core pressure drop is then made based on the difference between the sum of the individual channel flows and zero. Both the inner and outer

iterations are done using the Newton-Raphson method. Pressure changes in individual channels are calculated from the sum of the pressure changes in each axial block and include the effects of acceleration, friction, and buoyancy.

Tests of the model have been made for both pressurized and depressurized conditions for a few time steps to ensure that the detailed output calculations are being performed correctly. Simple starting conditions of five different uniform temperature regions have been used to check that reverse flow does indeed occur and that the individual channel flows sum to zero.

The next steps in the model development include incorporation of models of the side reflector, upper plenum, and lower plenum to permit decay heat transients to be run assuming the PCRV liner cooling system is the only heat sink available. Later changes will include modeling radial conduction between regions and natural convection loops through the steam generator modules and/or CACS modules.

6. Flow Distribution Model (G. Willcutt)

A model has been developed and tested for determining the flow distribution in multichannel parallel paths. The model will be used in the CHAP code to calculate the flow split through the core, side reflector, steam generator shroud, CACS, and CACS shroud. The flow split is determined iteratively by supplying flows to the CHAP code which returns pressure drops. New flows are then estimated based on the pressure drops and mass conservation. The process is repeated until the pressure drops all converge within an input tolerance. The flow distribution is determined using an implicit Newton-Raphson approach requiring matrix inversion.

Tests were made outside the CHAP code for two five-channel cases using pressure drop equations with linear, square, and cubic flow dependence, including simulated buoyancy terms, for both large flow and no net flow conditions. Tests were made with very poor initial flow guesses and in all cases the model converged in 17 or fewer iterations.

7. Three-Surface Thermal Radiation Model (G. Willcutt)

A general three-surface thermal radiation model has been developed, programmed, and checked on sample cases. The model solves the radiation network equations for arbitrary surface emissivities and areas. It produces coefficients which can then be used with the surface temperatures to calculate the radiation heat transfer in the HTGR upper and lower plenums. The radiation network was solved in two different ways to check the results and the results were also checked with a hand calculation for a sample case with black surfaces.

8. Boiling Heat Transfer Correlations (P. A. Secker)

We have developed a heat transfer coefficient model for CHAP to calculate an average tube-side heat transfer coefficient over the evaporator length in a once-through tube steam generator with uphill boiling. The model is based on integrating well established heat transfer correlations as a function of fluid quality over each quality range of interest.

In the evaporator four different boiling regimes are considered:

(a) nucleate boiling,
(b) forced convection vaporization,
(c) transition boiling, and
(d) stable film boiling.

Throughout the CHAP steam generator model, subcooled liquid and superheated vapor heat transfer correlations (corresponding to the economizer and superheater sections) are based on the Dittus-Boelter forced convection relationship

$$h = 0.023\left(\frac{k}{D_e}\right)\left(Re\right)^{.8}\left(Pr\right)^{.4} \qquad (33)$$

where

k is the fluid conductivity (liquid or vapor),

D_e is the channel equivalent diameter,

Re is the fluid Reynolds number, and

Pr is the fluid Prandtl number.

This correlation is modified as suggested by GAC to account for tube curvature effects.

In the evaporator section, heat transfer correlations are not so easily defined. Figure 43 is a qualitative graph which presents the heat transfer coefficient at a specific location as a function of the local quality. Because heat is continuously added to the fluid, the quality monotonically increases with distance from the evaporator entrance (onset of nucleate boiling).

In the nucleate boiling regime the quality of the fluid is generally well below 1% with as much as 50% of the volume fraction being vapor due to the creation of bubbles or plugs.

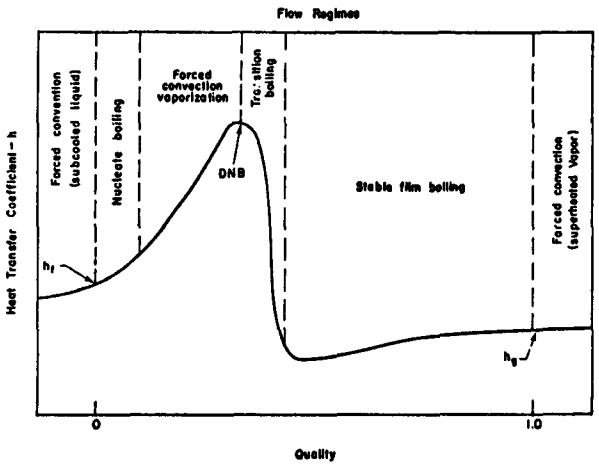

Fig. 43. Boiling water heat transfer coefficient vs quality.

Heat transfer correlations in this regime are generally based on the fluid saturation pressure and the wall-to-fluid temperature difference. The specific relationships are not incorporated in our model. Instead we assume that the next boiling regime (forced convection vaporization or annular flow) begins at a quality of 1%. A linear increase in the heat transfer coefficient is assumed between 0 and 1%

$$h_{NB}(x) = h_f + \left(h_{FCV_{.01}} - h_f\right)\left(x/.01\right) \qquad (34)$$

where

x is the fluid quality,

h_f is the heat transfer coefficient given in Eq. (33) at the evaporator entrance, and

$h_{FCV_{.01}}$ is the heat transfer coefficient in the forced convection vaporization regime at a quality of 1%.

In the forced convection vaporization regime (or annular flow) the wall of the tube is covered by a thin film of liquid and heat is transferred through this liquid film. In the center of the tube, vapor is flowing faster than the liquid and vapor is created primarily by vaporization from the liquid-vapor interface. In addition to the liquid in the annulus at the wall, there is a significant amount of liquid dispersed in the vapor as droplets.

The recommended[69] heat transfer correlation in this regime was developed by Schrock and Grossman[70] and is given by

$$h_{FCV}(x) = 2.5\, h_f \left(\frac{\rho_f}{\rho_g}\right)^{.375}\left(\frac{\mu_g}{\mu_f}\right)^{.075}\psi(x) \qquad (35)$$

where the subscript f refers to saturated liquid,

the subscript g refers to saturated vapor,

ρ is the fluid density,

μ is the fluid viscosity, and

the function $\psi(x)$ is given by

$$\psi(x) = (1 - x)^{.125}\, x^{.675} \quad . \qquad (36)$$

The completion of the annular-flow regime is characterized by departure from nucleate boiling (DNB). In annular flow the liquid film normally covers and cools the heating surface. The boiling crisis occurs when the liquid film becomes too thin and breaks down leaving dry patches (dryout). Dryout characterizes the transition boiling regime and begins at what is commonly called the critical heat flux (CHF). Correlations have been developed to predict CHF and the corresponding dryout quality. Heat transfer in the transition region is primarily via conduction through the vapor (low conductivity) resulting in a sharp decrease in the heat transfer coefficient. The dryout process occurs over a small quality range generally less than 1% in width.

In the CHAP model, CHF correlations[69] are used to predict the quality at DNB. We assume that the next boiling regime, stable film boiling, begins at a quality 1% higher than the quality at DNB. A linear variation in the heat transfer coefficient is then assumed over the transition region.

Heat transfer in the stable film boiling regime is from the hot wall to the vapor then to the liquid droplets. Vaporization actually occurs in the interior of the channel and not at the wall. Above the dryout quality the recommended[71] heat transfer coefficient for stable film boiling from Micropolskii is used. It is based on the saturated vapor coefficient modified to account for two-phase effects. The equation used is

$$h_{SFB}(x) = h_g\left[\frac{\rho_g}{\rho_f}\,(1-x) + 1\right]^{1.2} \qquad (37)$$

where h_g is the heat transfer coefficient given by Eq. (33) at the evaporator exit.

The average heat transfer coefficient in the evaporator section is obtained by integrating the above relationships over the appropriate quality ranges. It can be reduced to a relationship which is a function of the saturation pressure, the dryout quality, the mass flow rate, and the geometry of the channel:

$$\bar{h}_{ev} = \frac{\phi(P_{sat},\, X_{DNB})\, W^{.8}}{D_e^{1.8}} \qquad (38)$$

where

- W is the mass flow rate,
- D_e is the channel equivalent diameter,
- P_{sat} is the saturation pressure, and
- X_{DNB} is the dryout quality.

The bivariate function $\phi(P_{sat}, X_{DNB})$ has been evaluated for saturation pressures ranging from 700 kPa (approximately 100 psia) up to the critical pressure, and dryout qualities from 0.0 to 1.0. Figure 44 is a plot of the manifold formed by ϕ determined from a water properties computer code named WATER.[72]

We have created a matrix using equal grid spacings in P_{sat} and X_{DNB} containing 132 values of ϕ corresponding to the grid crossings shown in Fig. 44. The evaluation of ϕ is made with a simple bilinear interpolation polynomial using the four neighboring points given P_{sat} and X_{DNB}. The evaluation is extremely fast and accurate to within 1% (relative to the defining relationships) over the entire manifold.

9. Natural Convection Literature Search (G. Willcutt)

Approximately 400 references on natural convection were compiled on index cards for geometries, flow regimes, and

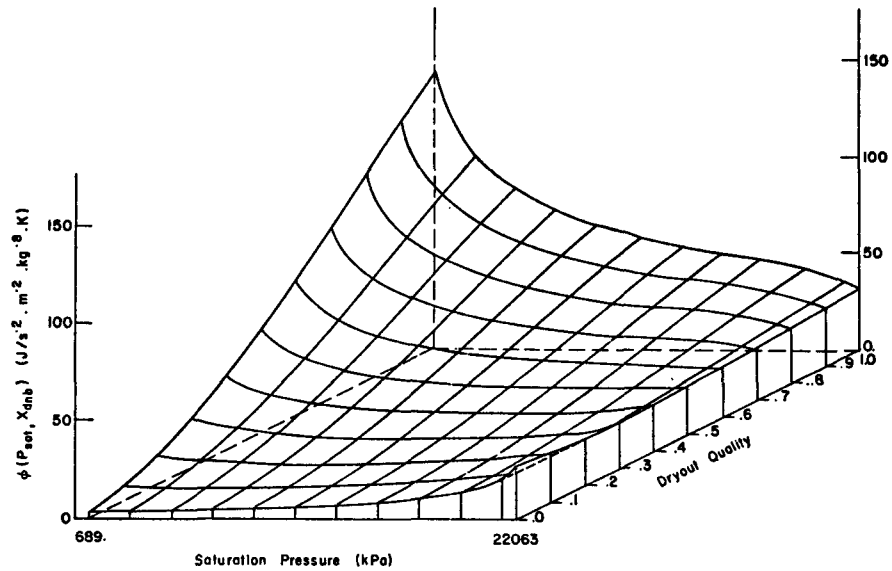

Fig. 44. The manifold of $\phi(P_{sat}, X_{DNB})$.

---

modeling approaches related to HTGR loss-of-forced-cooling modeling and other nuclear power applications. A key word master file was developed based on a title and abstract review, and a short computer program was written to produce a list of all references by author and reference number for each key work. A compilation was begun from the most relevant reference of correlations, analytical approaches, and computer models for expected applications in HTGR modeling.

REFERENCES

1. C. L. Smith, "Fuel Particle Behavior Under Normal and Transient Conditions," General Atomic Company report GA-A12971 (October 1, 1974).

2. GASSAR 6, General Atomic Standard Safety Analysis Report, General Atomic Company report GA-A13200, Vol. 1, Chapt. 2, Appendix 2A, Fig. 2A.3-4.

3. M. H. Schwartz, D. B. Sedgley, and M. M. Mendonca, "SORS: Computer Programs for Analyzing Fission Product Release from HTGR Cores During Temperature Excursions," General Atomic Company report GA-A12462, Fig. 5-1 (April 1974).

4. W. L. Kirk, "HTGR Safety Research Program, April-June 1975," Los Alamos Scientific Laboratory report LA-6054-PR, p. 3-7 (September 1975).

5. R. G. Lawton, "The AYER Heat Conduction Computer Program," Los Alamos Scientific Laboratory report LA-5613-MS (May 1974).

6. J. E. Foley, "^{131}I Release from an HTGR During the LOFC Accident," Los Alamos Scientific Laboratory report LA-5893-MS, p. 10 (March 1975).

7. Fred A. Siliday, General Atomic Company, personal communication, May 1975.

8. R. J. Pearce, R. A. U. Huddle, and P. Kofstad, "Fundamental Aspects of the Interaction of HTR Helium with Metal and Alloys," Atomic Energy Establishment, Winfrith, Dorchester, England report DPTN/522 (January 1974).

9. W. Betteridge and H. G. Bates, "A Multi-Purpose Instrument for Electrochemical Studies," Atomic Energy Establishment, Winfrith, Dorchester, England report DP-report-903, (December 1974).

10. R. J. Pearce and R. J. Thomas, "Examination of Metallic Specimens Exposed in Fuel Element Assemblies of the Dragon Reactor," Atomic Energy Establishment, Winfrith, Dorchester, England report RD/B/N 2025 (June 1971).

11. H. G. A. Bates, "The Influence of Impure Helium on Properties of Some Austenitic Steels," Atomic Energy Establishment, Winfrith, Dorchester, England report DP-report-934, (May 1975).

12. H. L. Langhaar, Dimensional Analysis and Theory of Models (J. Wiley and Sons, New York 1951).

13. O. C. Zienkiewicz, The Finite Element Method in Engineering Science (McGraw Hill, London, 1971).

14. P. H. Wirsching and J. T. P. Yao, "Random Behavior of Columns," Journal of the Engineering Mechanics Division, Proc. ASCE, June 1971.

15. A. Gurpinar and J. T. P. Yao, "Design of Columns for Seismic Loads," Journal of the Structural Division, Proc. ASCE, September 1973.

16. H. C. Martin, "On the Derivation of Stiffness Matrices for the Analysis of Large Deflection and Stability Problems," University of Washington, College of Engineering Report 66-4, (June 1966).

17. M. Watabe, "SIMEAR-Simulated Earthquake,"Program Documentation obtained from University of California, National Information Service, Earthquake Engineering Computer Program Applications.

18. S. Adham, A. Bhaumik, and J. Isenberg, "Reinforced Concrete Constitutive Relations," Air Force Weapons Laboratory report, Kirtland AFB, Albuquerque, New Mexico, AFWL-TR-74-72 (February 1975).

19. J. E. Carden, "Radio-release in Review with Special Emphasis on ^{85}Kr Clathrates and Kryptonates," Oak Ridge National Laboratory report ORNL-IIC-18, (July 1969).

20. D. Chleck, R. Maehl, O. Cucchiara, and E. Carnevale, "Radioactive Kryptonates," Inst. J. of Applied Radiation and Isotopes, Vol. 14, 1963, p. 581-610.

21. L. R. Zumwalt, North Carolina State University, private communication, August, 1975.

22. D. Chleck, Panametrics, Inc., Waltham, Massachusetts, private communication, September 1975.

23. J. Sattizahn, Los Alamos Scientific Laboratory, private communication, September and October, 1975.

24. E. Bryant, Los Alamos Scientific Laboratory, private communication, October 1975.

25. J. Roll, Westinghouse Electric Corp., private communication, October 1975.

26. W. Henninger, Westinghouse Electric Corp., private communication, October 1975.

27. G. Rymer, Westinghouse Electric Corp., private communication, October 1975.

28. G. A. Cowan and C. J. Orth, "Diffusion of Fission Products at High Temperatures from Refractory Matrices," Second United Nations International Conference on Peaceful Uses of Atomic Energy, 1958, Vol. 7 p. 328-334.

29. G. T. Rymer, G. L. Grandy, W. A. Henninger, and J. A. Roll, "Interim Report on Fission Product Release from NERVA Fuel During Post-Irradiation Thermal Anneals and During NRX-A2 Test," Westinghouse Astronuclear Laboratory report WANL-TME-1165, (May 1965).

30. T. Nakai, S. Yajima, K. Shiha, J. Osugi, and D. Shinoda, "The Behavior of Fission Products Captured in Graphite by Nuclear Recoil II. The Diffusion of Xenon-135 in Graphite at a High Temperature," Bull. Chem. Soc. Japan Vol. 33, No. 4, p. 497-501 (1960).

31. G. T. Rymer, W. A. Henninger, and G. L. Grandy, "The Release of Fission Products from UC_2 Graphite Fuels," Westinghouse Electric Corp. Astronuclear Laboratory report WANL-TME-542, (August 1963).

32. G. T. Rymer, W. A. Henninger and G. L. Grandy, "Interim Report on the Release of Fission Products from NERVA Fuel," Westinghouse Astronuclear Laboratory report WANL-TNR-162, (September 1964) and WANL-TNR-142, (July 1964).

33. W. A. Henninger, J. Roesmer, and G. T. Rymer, "Fission Product Release from NERVA Fuels-A Summary," Westinghouse Astronuclear Laboratory report WANL-TME-1896 (January 1969).

34. R. P. Thorne, V. C. Howard, and B. Hope, "Radiation-induced Changes in Porous Cubic Silicon Carbide," Proc. British Ceramic Soc. No. 7, p. 449-459 (February 1967).

35. R. J. Price, "Annealing Behavior of Neutron-Irradiated Silicon Carbide Temperature Monitors," Nuclear Technology, Vol. 16, p. 536-542 (December 1972).

36. H. Suzuki, T. Iseki, and M. Ito, "Annealing Behavior of Neutron Irradiated β-SiC," J. of Nuclear Materials, Vol. 48, p. 247-252 (1973).

37. W. H. Martin, and A. M. Price, "Determination of Dose and Temperature in Graphite Irradiation Experiments in the Dounreay Fast Reactor," J. of Nuclear Energy, Vol. 21, p. 359-371 (1967).

38. N. F. Pravdyuk, V. Nikolaenko, V. Karpuchin, and V. Kuznetsov, "Investigation of Diamond and Silicon Carbide as Indicators of Irradiation Conditions," Properties of Reactor Materials and the Effects of Radiation Damage, D. J. Littler, Editor (Butterworth, 1962).

39. D. G. Hurst, "Diffusion of Fission Gas — Calculated Diffusion from a Sphere Taking Into Account Trapping and Return from the Traps," Atomic Energy of Canada Limited, Chalk River, Ontario, report, CRRP-1192, AECL-1550, (November 15, 1962).

40. "Reactor Safety Study - An Assessment of Accident Risks in U.S. Commercial Nuclear Power Plants," U.S. Atomic Energy Commission, WASH-1400 (Draft), (August 1974).

41. M. G. Stamatelatos, R. J. LaBauve, and J. C. Vigil, Nuclear Data Processing for HTGR Safety Research in "Quarterly Report on Transport Theory, Reactor Theory and Reactor Safety for the Period April 1 - June 30, 1975," Los Alamos Scientific Laboratory report, LA-6029-PR, p. 18-21 (August 1975).

42. B. J. Toppel, A. L. Rago, and D. M. O'Shea, "MC^2, A Code to Calculate Multi-group Cross Sections," Argonne National Laboratory report ANL-7318 (1967).

43. W. W. Clendenin, "Calculation of Thermal Neutron Diffusion Length and Group Cross Sections: The GLEN Program," Los Alamos Scientific Laboratory report LA-3893 (1968).

44. W. W. Clendenin, "Calculation of Thermal Neutron Scattering Cross Sections for Crystalline Materials: The TOR Program," Los Alamos Scientific Laboratory report LA-3823 (1967).

45. Y. D. Naliboff and J. U. Koppel, "HEXSCAT, Coherent Elastic Scattering of Neutrons by Hexagonal Lattices," General Atomic report GA-6026 (1964).

46. D. R. Harris, R. J. LaBauve, R. E. McFarlane, P. D. Soran, C. R. Weisbin and J. E. White, "MINX, A Modular Code System for Processing Multigroup Cross Sections from Nuclear Data in ENDF/B Format," Proc. of Seminar on Codes for Nuclear Data Processing, NEA-CPL Ispra (1973).

47. R. W. Hardie and W. W. Little, Jr., "1DX, A One-Dimensional Diffusion Code for Generating Effective Nuclear Cross Sections," Battelle Northwest Laboratory report, BNWL-954 (1969).

48. R. J. LaBauve, Los Alamos Scientific Laboratory, unpublished data, 1975.

49. P. Wälti, "Evaluation of Grain Shielding Factors for Coated Fuel Particles," Nucl. Sci, Engr. 45, 321-330 (1971).

50. P. Wälti and P. Koch, "MICROX, A Two-Region Flux Spectrum Code for the Efficient Calculation of Group Cross Sections," Gulf General Atomic report GA-A10827 (1972).

51. C. A. Stevens and C. V. Smith, "GAROL, A Computer Program for Evaluating Resonance Absorption Including Resonance Overlap," General Atomic report GA-6637 (1965).

52. D. R. Mathews, P. K. Koch, J. Adir, and P. Wälti, "GGC-5, A Computer Program for Calculating Neutron Spectra and Group Constants, Gulf General Atomic report GA-8871 (1971).

53. K. M. Case, F. De Hoffman, and G. Placzek, Introduction to the Theory of Neutron Diffusion, U.S. Government Printing Office, Washington, D.C. (1953).

54. I. Carlvik, "Dancoff Correction in Square and Hexagonal Lattices," Aktiebolaget Atomenergi report AE-257 (1966).

55. I. Carlvik and B. Pershagen, "The Dancoff Correction in Various Geometries," Aktiebolaget Atomenergi report AE-16 (1959).

56. E. P. Wigner, E. Creutz, H. Jupnik and T. Snyder, "Resonance Absorption of Neutrons by Spheres," J. Appl. Phys. 26, 260 (1955).

57. M. M. Levine, "Resonance Integral Calculations for ^{238}U Lattices," Nucl. Sci. and Engr. 16, 271 (1963).

58. J. N. Otter, "Escape Probability Approximations in Lumped Resonance Absorbers," Atomics International report NAA-SR-9744 (1964).

59. G. I. Bell, Nuclear Reactor Theory (Van Nostrand Reinhold Company, New York, 1970).

60. L. Dresner, Resonance Absorption in Nuclear Reactors (Pergamon Press, New York 1960).

61. J. C. Vigil, "Beginning-of-Life Neutronic Analysis of a 3000 MW(t) HTGR," Los Alamos Scientific Laboratory report (to be published).

62. K. D. Lathrop (Person-in-Charge), "Quarterly Report on Transport Theory, Reactor Theory, and Reactor Safety, January 1 - March 31, 1975," Los Alamos Scientific Laboratory report LA-5964-PR (June 1975).

63. K. D. Lathrop, "DTF-IV, a FORTRAN-IV Program for Solving the Multigroup Transport Equation with Anisotropic Scattering," Los Alamos Scientific Laboratory report LA-3373 (1965).

64. P. A. Secker and J. S. Gilbert, "Status of CHAP: Composite HTGR Analysis Program," Los Alamos Scientific Laboratory report, (to be published).

65. B. M. Carmichael, "Standard Interface Files and Procedures for Reactor Physics Codes, Version III," LA-5486-MS (February 1974).

66. J. B. Payne, Los Alamos Scientific Laboratory, unpublished data, 1966.

67. C. Wm. Gear, Numerical Initial Value Problems in Ordinary Differential Equations, (Prentice Hall, 1971).

68. J. J. Lucas and J. V. Wait, "DARE-P User's Manual," University of Arizona, CSRL report 255, (December 1974).

69. L. S. Tong, "Boiling Crisis and Critical Heat Flux," AEC Critical Review Series, TID-25887 (1972).

70. V. E. Schrock and L. M. Grossman, "Forced Convection Boiling Studies, Final Report on Forced Convection Vaporization Project," AEC report TID-14632

71. Z. L. Miropolskii, "Heat Transfer in Film Boiling of a Steam-Water Mixture in Steam Generating Tubes," USAEC report AEC-TR-6252 (1963).

72. W. A. Coffman and L. L. Lynn, "WATER: A Large Range Thermodynamic and Transport Water Property FORTRAN-IV Computer Program," Bettis Atomic Power Laboratory report WAPD-TM-568 (December 1968).